

# Solar-driven efficient methane catalytic oxidation over epitaxial ZnO/La<sub>0.8</sub>Sr<sub>0.2</sub>CoO<sub>3</sub> heterojunctions

Ji Yang<sup>a, †</sup>, Wen Xiao<sup>b, †</sup>, Xiao Chi<sup>c,f</sup>, Xingxu Lu<sup>d</sup>, Siyu Hu<sup>a</sup>, Zili Wu<sup>e</sup>, Wenxiang Tang<sup>d</sup>, Zheng Ren<sup>d</sup>, Sibow Wang<sup>d</sup>, Xiaojiang Yu<sup>c</sup>, Lizhi Zhang<sup>a</sup>, Andriwo Rusydi<sup>c,g</sup>, Jun Ding<sup>b</sup>, Yanbing Guo<sup>a,\*</sup>, Pu-Xian Gao<sup>d,\*</sup>

<sup>a</sup>Key Laboratory of Pesticide & Chemical Biology of Ministry of Education, Institute of Environmental and Applied Chemistry, College of Chemistry, Central China Normal University, Wuhan 430079, People's Republic of China

<sup>b</sup>Department of Materials Science and Engineering, National University of Singapore, 117575, Singapore

<sup>c</sup>Singapore Synchrotron Light Source, National University of Singapore, 5 Research Link, 117603, Singapore

<sup>d</sup>Department of Materials Science and Engineering & Institute of Materials Science, University of Connecticut, Storrs, CT 06269-3136, USA

<sup>e</sup>Chemical Science Division and Center for Nanophase Materials Sciences, Oak Ridge National Laboratory, Oak Ridge, TN 37831, United States

<sup>f</sup>Department of Chemistry, National University of Singapore, 3 Science Drive 3, 117543, Singapore

<sup>g</sup>Department of Physics, 2 Science Drive 3, National University of Singapore, 117542, Singapore

<sup>†</sup>Those authors contribute equally to this work.

\*To whom correspondence should be addressed. E-mail: [guoyanbing@mail.ccnu.edu.cn](mailto:guoyanbing@mail.ccnu.edu.cn); [puxian.gao@uconn.edu](mailto:puxian.gao@uconn.edu)

## Highlights

1. Solar driven efficient methane oxidation is firstly proved under high velocity continuous flow.
2. Epitaxial hetero-interface design concept is proposed for the fabrication of platinum group metal free oxidation catalysts.

3. Surface lattice oxygen replenishment mechanism through epitaxial interface electron transfer is identified and elucidated.
4. The synergy of photothermal effect and photo-promoted electron transfer results in about 2 times higher CH<sub>4</sub> oxidation activity than thermal catalysis system.

## **Abstract**

Gas flaring in oil/gas drilling and gas leakage in natural gas power plant lead to significant energy loss and environmental burden. Here, solar-driven efficient methane oxidation was demonstrated under high velocity continuous flow over the ZnO/La<sub>0.8</sub>Sr<sub>0.2</sub>CoO<sub>3</sub> (ZnO/LSCO) heterojunctions. The ZnO/LSCO heterojunctions enabled a unique epitaxial hetero-interface, which effectively regulated the electron transfer between Zn *3d*-O *2p* hybrid orbital in ZnO and Co *e<sub>g</sub>* orbital in LSCO and promoted the rapid generation and refill of oxygen vacancy with unpaired electron (V<sub>o</sub>•), thus enhancing the activity and mobility of surface lattice oxygen in ZnO/LSCO. Under solar illumination, the synergy of photothermal and photocatalytic effect boosted the reversible electron transfer in the interface, which further activate surface lattice oxygen, resulting in a ~2 times higher methane oxidation activity. Such a solar-driven system not only enables a promising pathway for emitted methane utilization, but also provides an advanced catalyst design concept of epitaxial interface construction.

**Keywords:** Solar-driven methane oxidation; Epitaxial hetero-interface; Reversible Electron transfer; Photothermal effect; Photo-excited electrons

## **1. Introduction**

Methane, the principal component of natural gas, is the highest mass energy density fuel among carbon-based energy source being produced and in huge reserve. Accompanied with the shale gas revolution and fire ice discovery, the use of natural gas, as substantial cleaner fuel and chemical feedstock becomes more and more feasible [1]. However, it was estimated that as much as 140 billion cubic meters of unusable natural gas were vented or flared each year in oil and gas drilling from 2013 to 2017 [2,3], which is equivalent to 25 % of the United States' gas or 30% of Europ Union

annual consumption [4]. Natural gas (methane) venting is a big challenge to global warming, with 25 times higher green house effect than CO<sub>2</sub>, and gas flaring is accompanied by the production of toxic NO<sub>x</sub>. This thus leads to significant energy loss, undesirable pollutants and human health risk. Therefore, more efficient strategy and devices for methane emission control are in urgent demand in those industrial applications for better environmental benefit.

Catalytic oxidation of methane with Pd catalysts is a clean and practical alternative [5] but suffers from the high cost associated with Pd and the extra fuel consumption needed to heat up the system [6]. Recently, taking the full advantage of abundant solar energy, both selective catalytic oxidation [7] and total oxidation of methane under sunlight illumination [8] have been reported. But comparing with the traditional thermal catalysis, the several orders of magnitude lower reaction rate, the low solar harvesting efficiency and fast recombination of the photogenerated electron-hole pairs of photocatalytic process limited its application in the high velocity condition such as gas flaring [9–15]. While photothermal catalytic process, in which photon energy dissipated into heat induced by surface plasmon resonance absorption to promote the catalytic reaction [16], has been proved to be able to adopted in various industrial processes such as Fischer-Tropsch synthesis [17], CO<sub>2</sub> hydrogenation [18,19], volatile organic chemicals (VOCs) elimination [20,21]. However, solar assisted heterogeneous catalytic oxidation of methane at high space velocity condition has seldomly been demonstrated, and the synergy of photocatalytic and photothermal effect on catalytic oxidation of methane also has not been illustrated.

To fully leverage the solar promoted performance and elucidate the synergy of photothermal catalysis and photocatalysis on methane oxidation, a composite catalyst including photothermal catalysts, which can effectively activate methane, and rational designed interface, which can enable efficient charge transfer [22–27], would be ideal. Perovskite oxide [28,29], promising noble metal free catalysts for catalytic methane oxidation, is also an excellent photo-thermal materials due to its characteristic of well-defined IR-absorption capability derived from free Jahn-Teller hole polarons and Jahn-

Teller hole polarons within localized charge transfer vibronic excitons [30–32]. It is inspired that a well-designed metal oxide/perovskite interface would lead to an efficient catalysts for solar-driven CH<sub>4</sub> oxidation.

Herein, via rational metal oxide/perovskite interface design, solar-driven efficient methane oxidation over ZnO/La<sub>0.8</sub>Sr<sub>0.2</sub>CoO<sub>3</sub> (ZnO/LSCO) heterojunction catalysts was demonstrated under high space velocity continuous flow. The hetero-epitaxial interface of ZnO/LSCO, constructed by simultaneously bonding Co<sup>3+</sup>, Sr<sup>2+</sup> and La<sup>3+</sup> in LSCO (-110) planes with O<sup>2-</sup> in ZnO (01-10) planes, enabled a synergy of photocatalytic and photothermal catalytic effect and resulted in a much higher solar-driven catalytic activity than control catalysts with no interface. The characteristic interface effectively regulated the electron transfer between Zn 3d-O 2p hybrid orbital in ZnO and Co e<sub>g</sub> orbital in LSCO and promoted the rapid generation and refill of oxygen vacancy with unpaired electron (V<sub>o</sub>•), thus enhancing the activity and mobility of surface lattice oxygen in ZnO/LSCO. Under solar illumination, the produced heat via photothermal effect promoted transform of ZnO/LSCO from heterojunction to Schottky junction. The synergy of photothermal and photocatalytic effect boosted reversible electron transfer on the interface, which further promoted the amount of surface active lattice oxygen and corresponding fast replenishment, resulting in a higher methane oxidation activity. The catalysts design concept demonstrated here shows great potential for the solar energy utilization and the control of carbon footprint in industrial process. Furthermore, the fundamental heterojunction catalysts design concept and active oxygen replenishment mechanism uncovered here provides a new approach for the design and fabrication of efficient PGM free oxidation catalysts.

## **2. Experimental section**

### *2.1 Density functional theory (DFT) calculations*

For this work, first-principles calculations are performed using Vienna ab initio simulation package (VASP) [33] based on density functional theory (DFT). The electron-ion interactions are modelled by employing projector augmented wave (PAW)

[34] potentials. Exchange and correlation effects for structure relaxation are approximated by generalized gradient approximation (GGA) [35], using Perdew-Burke-Ernzerhof (PBE) functional [36]. The cutoff energy is set at 400 eV for the plane-wave basis restriction in all calculations. K-points are sampled under Monkhorst-Pack scheme [37] for the Brillouin-zone integration. In all calculations, the forces acting on all atoms are  $<0.02$  eV/Å in fully relaxed structures and self-consistency accuracy of  $10^{-4}$  eV is reached for electronic loops.

According to previous report [38], in our simulation, the relation  $5\mu_{\text{La}}+1\mu_{\text{Sr}}+6\mu_{\text{Co}}+18\mu_{\text{O}}=E_{\text{La}_5\text{Sr}_1\text{Co}_6\text{O}_{18}}$  has to be satisfied so that La, Sr, Co and O reservoirs are at thermodynamic equilibrium with bulk  $\text{La}_5\text{Sr}_1\text{Co}_6\text{O}_{18}$ , where  $E_{\text{La}_5\text{Sr}_1\text{Co}_6\text{O}_{18}}$  is the total DFT energy of bulk  $\text{La}_5\text{Sr}_1\text{Co}_6\text{O}_{18}$ . The actual oxygen chemical potential  $\mu_{\text{O}}$  depends on experimental synthesis conditions ranging from O-poor conditions to O-rich conditions. In O-poor condition,  $\mu_{\text{O}}$  is obtained by  $\mu_{\text{O}}=\frac{1}{18}[E_{\text{La}_5\text{Sr}_1\text{Co}_6\text{O}_{18}}-5E_{\text{La}}^{\text{metal}}-1E_{\text{Sr}}^{\text{metal}}-6E_{\text{Co}}^{\text{metal}}]$ , where  $E_{\text{La}}^{\text{metal}}$ ,  $E_{\text{Sr}}^{\text{metal}}$  and  $E_{\text{Co}}^{\text{metal}}$  are the total DFT energies of a La, Sr and Co atom in metallic La, Sr and Co respectively. On the other extreme,  $\mu_{\text{O}}$  in O-rich conditions is used as the reference and the upper bound of  $\mu_{\text{O}}=\frac{1}{2}E_{\text{O}_2}$  is set at 0 eV, where  $E_{\text{O}_2}$  is the total energy of an oxygen molecular in a large box. This condition sets the lower bound of  $\mu_{\text{O}}$  to be -4.375 eV. Based on the above, the formation energy of an oxygen vacancy is calculated by  $E_{\text{F}}^{\text{Vo}}=E_{\text{tot}}^{\text{Vo}}-E_{\text{tot}}^{\text{no Vo}}+\mu_{\text{O}}$ , where  $E_{\text{tot}}^{\text{Vo}}$  and  $E_{\text{tot}}^{\text{no Vo}}$  are the total DFT energies of a system with and without an oxygen vacancy. The charge density difference is obtained by  $\Delta\rho=\rho_{\text{ZnO/LSCO}}-\rho_{\text{LSCO}}-\rho_{\text{ZnO}}$ , where  $\rho_{\text{ZnO/LSCO}}$ ,  $\rho_{\text{LSCO}}$  and  $\rho_{\text{ZnO}}$  are the total charge densities of the interface model, the corresponding individual LSCO slab and ZnO slab respectively.

## 2.2 Materials

Zinc acetate dihydrate ( $\text{Zn}(\text{CH}_3\text{COO})_2 \cdot 2\text{H}_2\text{O}$ ), Lanthanum nitrate hexahydrate ( $\text{La}(\text{NO}_3)_3 \cdot 6\text{H}_2\text{O}$ ), Strontium nitrate ( $\text{Sr}(\text{NO}_3)_2$ ), Cobaltous nitrate ( $\text{Co}(\text{NO}_3)_2$ ), N, N-

Dimethylformamide (DMF), Hexamethylenetetramine (HMT, 99%), Polyvinylpyrrolidone (Mw: 55000), Diethanolamine, Ammonium hydroxide ( $\text{NH}_3 \cdot \text{H}_2\text{O}$ ), Tetraethyl orthosilicate (TEOS, 98%) and Ethanol were purchased from Sinopharm Chemical Reagent Co, Ltd.. All chemicals were used as received. The monolith cordierite (diameter: 1inch, height: 1cm, channel: 1 mm $\times$ 1 mm) substrate was provided by Corning cooperation.

### *2.3 Catalyst preparation*

#### *2.3.1 Growth of ZnO nanorod array*

ZnO nanorod array on 3-D monolith substrate were fabricated as reported [39]. The monolith cordierite was first cleaned by deionized water and ethanol in ultrasonic bath to remove the contaminants on substrate. Then the substrate was coated (via dip-coating) with zinc acetate (20 mmol) in ethanol solution for several times and annealed at 350 °C for 5 hours to form (002) face oriented ZnO seed layer. After coating of ZnO layer, ZnO nanorods growth was conducted by a hydrothermal process. Equal molar of  $\text{Zn}(\text{NO}_3)_2$  and hexamethylenetetramine (HMT) (25 mmol) were dissolved in deionized water (200 mL) as precursor. The pre-annealed substrate was then put in the prepared precursor at 80 °C for 6 hours. After three cycles of ZnO nanorod growth, the nanorods integrated substrate was rinsed in deionized water and cleaned in ultrasound bath with ethanol for 10 minutes. Finally, the sample was dried at 80 °C in air for further characterization.

#### *2.3.2 Fabrication of ZnO/SiO<sub>2</sub> core-shell nano-array*

A modified Stober process was used to produce a uniform coating of SiO<sub>2</sub> onto ZnO nanorod arrays [40]. Briefly, ZnO nanorod array was impregnated into (50 mL) ethanol.  $\text{NH}_3 \cdot \text{H}_2\text{O}$  (1.5 mL) was then added dropwise. TEOS (1.5 mL) was added by syringe and the reaction incubated for 8 hours while stirring.

#### *2.3.3 Fabrication of ZnO/La<sub>0.8</sub>Sr<sub>0.2</sub>CoO<sub>3</sub> (ZnO/LSCO) epitaxial heterojunction, ZnO/SiO<sub>2</sub>/LSCO nanorods and LSCO nanotube based monolithic catalysts*

The loading of  $\text{La}_{0.8}\text{Sr}_{0.2}\text{CoO}_3$  (LSCO) were conducted by the colloidal deposition method we have developed [41]. Firstly, the perovskite LSCO colloidal solution was prepared by dissolving stoichiometric (0.12 mol/L) lanthanum nitrate hexahydrate ( $\text{La}(\text{NO}_3)_3 \cdot 6\text{H}_2\text{O}$ ), strontium nitrate ( $\text{Sr}(\text{NO}_3)_2$ ), and cobaltous nitrate ( $\text{Co}(\text{NO}_3)_2$ ) in N, N-Dimethylformamide (DMF) (20 mL) in sonication. In the other bottle, polyvinylpyrrolidone (M.W 55,000) (2 g) and diethanolamine (0.5 mL) were dissolved in DMF (20 mL). Then the two solutions were mixed under vigorous stir at 60 °C and the solution turned dark brown. The solution was aged for 24 hours. Then, by using dip coating, a uniform LSCO coating layer could be made on the ZnO nanorod array monolith substrates and ZnO/SiO<sub>2</sub> nanorod array monolith substrates. This deposition process was repeat for a few cycles until the desired loading amount was acquired. Finally, the substrate was annealed at 700 °C for 2 hours to ensure good crystallinity after annealing treatment, and ZnO/LSCO epitaxial heterojunction and ZnO/SiO<sub>2</sub>/LSCO nanorods catalysts were obtained. LSCO nanotube integrated monolithic catalysts were fabricated by H<sub>2</sub> reduction of ZnO/LSCO epitaxial heterojunction at 600 °C for 3h [42]. It has been reported that reduced LSCO nanotube could be re-oxidized to the initial chemical state by annealing in O<sub>2</sub> atmosphere, including the amount of adsorbed oxygen and surface lattice oxygen [43].

#### *2.4 Characterization*

The morphology and structure of synthesized nano-array monolithic catalysts were examined by field emission scanning electron microscopy (FE-SEM, JEOL 6335F) and Transmission electron microscopy (TEM, JEOL JEM-2010F). The crystalline structure of a typical sample was analyzed by X-ray diffractometer (XRD, BRUKER AXS D5005) using  $\text{CuK}\alpha$  radiation of 1.540598Å. All measures were performed at room temperature.

The Brunauer-Emmett-Teller (BET) specific surface areas and pore size distributions were obtained on a Quantachrome NOVA 1000 Gas Sorption Analyzer and Micromeritics ASAP 2020 physisorption analyzer. X-ray photoelectron spectroscopy (XPS) was performed with a Kratos Analytical (Axis Ultra DLD)

instrument equipped with monochromatic Al K $\alpha$  source operating at 1486.7 eV. The signal was filtered with a hemispherical analyzer (pass energy 160 eV for survey spectra and 20 eV for narrow high resolution scans). The C 1s photoelectron line at 284.6 eV was used as an internal standard for correction of charging effects in all samples. Low-temperature EPR spectra were acquired on a Bruker EMX EPR spectrometer (Billerica, MA) at 77K. Diffuse reflectance UV–vis-IR absorption was measured on a PE950 spectrophotometer.

CO-TPR, TPD, and oxygen isotopic exchange over ZnO/LSCO and LSCO nanotube samples (ca. 30 mg) were also conducted on the AMI microreactor system (Altamira AMI-300). Before each of the experiments, the samples were pretreated in flowing 5%  $^{16}\text{O}_2/\text{He}$  (30 mL/min) at 673 K for 1 h and cooled down to room temperature (rt) and switched to helium purging for 30 min. For CO-TPR, the pretreated sample was exposed to 2% CO/2% Ar/He (30 mL/min) at rt for 30 min and then ramped (10 K/min) up to 1073 K and held for another 30 min. In CO-TPR, the gas stream product  $\text{CO}_2$  was analyzed by an online quadrupole mass spectrometer (QMS) (OmniStar GSD-301  $\text{O}_2$ , Pfeiffer Vacuum). For oxygen isotopic exchange, the pretreated sample was exposed to 1%  $^{18}\text{O}_2/\text{He}$  (30 mL/min) at rt and ramped (10 K/min) up to 1100 K. The oxygen isotopomers (32, 34, and 36) were monitored by the online QMS. X-ray absorption near edge structure (XANES) was collected at SINS beamline at the Singapore Synchrotron Light Source (SSLS).

## 2.5 Activity evaluation

### 2.5.1 Evaluation of thermally catalytic performance of methane oxidation

Thermally catalytic performance of the samples was measured in a BenchCAT 100RHP Hybrid reactor (Altamira Instruments) and 0.3 g catalyst samples were used. For  $\text{CH}_4$  combustion, the  $\text{O}_2$  concentration in the inlet was 20 % and  $\text{CH}_4$  concentration was 500 ppm / 1%. The balance of the gas was  $\text{N}_2$  and the total flow rate into the reactor was 10 and 50 sccm, giving a weight hour space velocity (WHSV) of around 40,000 and 200,000  $\text{mL g}^{-1}\text{h}^{-1}$  ( $\sim 1200, 6000 \text{ h}^{-1}$  for gas hour space velocity (GHSV),

respectively). Methane oxidation study was carried out in the temperature range of 250 °C-750 °C. An on-line gas chromatograph (GC, 9790, Taizhou) with a flame ionization detector (FID) was used for identification and quantification of the gas species in the product stream. For CO oxidation, the total flow rate of reactant feed (1% CO + 10 % O<sub>2</sub> + N<sub>2</sub> (balance)) was 50 sccm. The WHSV was controlled to be around 200,000 mL g<sup>-1</sup>h<sup>-1</sup> (~6000 h<sup>-1</sup> for GHSV). The total flow rate into the reactor was 50 sccm. CO oxidation study was carried out in a temperature range of 20 °C-500 °C. Products stream were analyzed on line by Agilent Micro GC. In terms of NO oxidation, the total flow rate of reactant feed (3% NO + 10% O<sub>2</sub> + N<sub>2</sub> (balance)) was 50 sccm, giving a WHSV of ca. 200,000 mL g<sup>-1</sup>h<sup>-1</sup> (~6000 h<sup>-1</sup> for GHSV). NO oxidation study was carried out in a temperature range of 20 °C - 500 °C. A FTIR were used as the detector to analyze product gas mixture.

### *2.5.2 Evaluation of photo-thermally catalytic performances of methane oxidation*

The photothermally catalytic activity evaluation of the samples for CH<sub>4</sub> oxidation was carried out in a designed quartz device [44]. Powder-tunable Xenon lamp (300 W) was used as simulated solar irradiation to trigger methane oxidation. 0.3 g catalyst samples were filled in the quartz reactor with an area of 2 cm<sup>2</sup>, and the position of the solar simulator was adjusted so that the focal point illuminated the catalyst area. The catalysis temperature was monitored by a catalyst-contact thermocouple. The reactant of 500 ppm CH<sub>4</sub> + 20% O<sub>2</sub> + N<sub>2</sub> (balance) was passed at a flow rate of 10 mL/min, giving a WHSV of around 40,000 mL g<sup>-1</sup>h<sup>-1</sup> (~1200 h<sup>-1</sup> for GHSV). The outlet gas compositions were analyzed with an on-line gas chromatograph (GC, 9790, Taizhou) with a flame ionization detector (FID).

## **3. Results and discussion**

### *3.1 Density functional theory (DFT) calculations for structure design of catalysts*

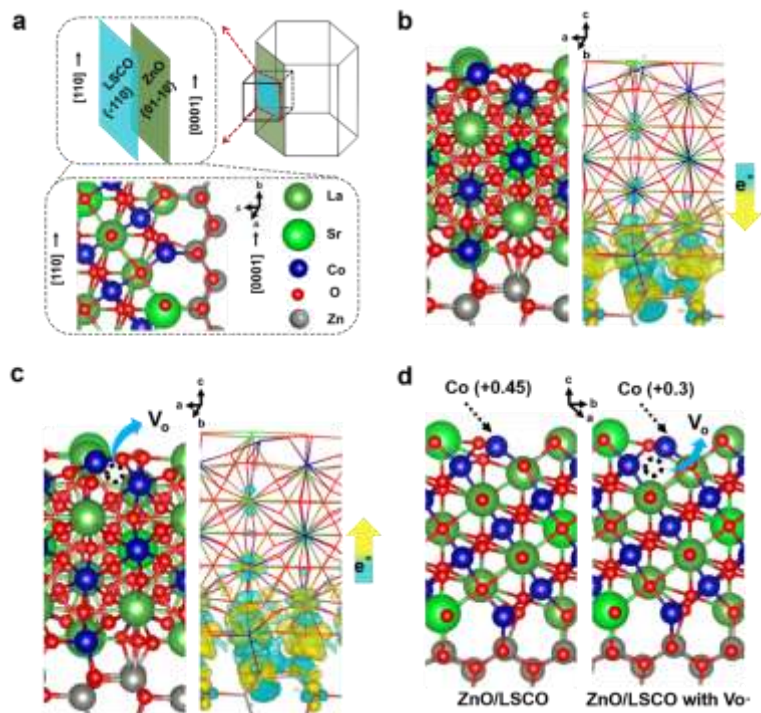


**Fig. 1.** (a) Atomic structure and schematic illustration of ZnO/LSCO epitaxial interface. Charge density difference caused by formation of ZnO/LSCO interface, where electron accumulation and depletion are represented by yellow ( $\Delta\rho = +1 \times 10^{-3} e \cdot \text{bohr}^{-3}$ ) and cyan ( $\Delta\rho = -1 \times 10^{-3} e \cdot \text{bohr}^{-3}$ ) respectively: (b) Pristine; (c) with  $V_o$ . (d) Bader charge analysis (valence state) of Co adjacent to  $V_o$  in pristine ZnO/LSCO and ZnO/LSCO with  $V_o$ .

For the structure design of LSCO catalysts, DFT calculations were firstly carried out to investigate the interface effect on surface reactivity of perovskite (Fig. 1). Based on our previous researches [41,45], the subtle lattice mismatching between ZnO and hexagonal phase  $\text{La}_{0.8}\text{Sr}_{0.2}\text{CoO}_3$  (LSCO) ( $d_{\text{ZnO}(002)} = 0.26 \text{ nm}$ ;  $d_{\text{La}_{0.8}\text{Sr}_{0.2}\text{CoO}_3(110)} = 0.27 \text{ nm}$ ) indicates that an epitaxial growth of ZnO/  $\text{La}_{0.8}\text{Sr}_{0.2}\text{CoO}_3$  (ZnO/LSCO) can be established by matching ZnO (01-10) planes and LSCO (-110) planes (Fig. 1a). As shown in Fig. 1a and Figure S1, DFT modeling results suggested  $\text{Co}^{3+}$ ,  $\text{Sr}^{2+}$  and  $\text{La}^{3+}$  in LSCO (-110) planes bonded simultaneously with  $\text{O}^{2-}$  in ZnO (01-10) planes. It has been evidenced that charge transfer of epitaxial interface would contribute to overall activity of catalytic reactions [46,47].  $\text{CH}_4$  oxidation over perovskites generally proceeds through Mars and van Krevelen (MvK) mechanism accompanied by the generation and

refilling of surface oxygen vacancies ( $V_{O\cdot}$ ) [48], in which  $V_{O\cdot}$  as a promoter plays a decisive role to affect catalytic performance of  $CH_4$  oxidation. To identify the charge redistribution evolution on ZnO/LSCO epitaxial interface without and with  $V_{O\cdot}$  on LSCO exposed surface, the charge density difference (the quantity difference of charge per unit cell volume) was calculated by DFT calculations. The theoretical calculation results suggest that the characteristic ZnO/LSCO interface acts as an “electron regulator” and promotes a reversible electron transfer. At first, ZnO tends to withdraw electron from surface Co in LSCO (Fig. 1b), so that O connected with Co can be activated and easily removed to generate  $V_{O\cdot}$ . After  $V_{O\cdot}$  are present in Fig. 1c, ZnO will in turn provide electrons to surface Co. Thus the reducibility of cobalt ions is enhanced and the adjacent  $V_{O\cdot}$  can be readily filled by dissociated oxygen. Moreover, Bader charge analysis is performed on Co adjacent to  $V_{O\cdot}$  in pristine ZnO/LSCO and ZnO/LSCO with  $V_{O\cdot}$  (Fig. 1d), which also affirms that electrons ( $0.15 e^-$ ) transfer to Co after generating  $V_{O\cdot}$ .

### 3.2 Catalysts characterization

On the basis of theoretical model, a series of perovskite monolithic catalysts with or without epitaxial interface were then fabricated. As shown in Figure S2a, ZnO/LSCO epitaxial heterojunction model catalysts were firstly *in-situ* grown onto commercial honeycomb substrates ( $1\text{ cm}\times 2\text{ cm}\times 2\text{ cm}$ ) in the form of array structure via a facile solution method [42]. It can be observed from Figure S2b that ZnO/LSCO monolithic catalysts exhibits bright metallic black color throughout the substrate, which indicates the uniform coating of ZnO/LSCO nano-array on the monolith. As control samples without epitaxial interface, LSCO nanotube was fabricated by reducing the ZnO/LSCO in 10%  $H_2/N_2$  around  $600\text{ }^\circ\text{C}$  for 3 hours [42] and ZnO/SiO<sub>2</sub>/LSCO nanorods (chemically inert SiO<sub>2</sub> as electron blocker between ZnO and LSCO) were also *in-situ* grown onto commercial monolithic substrates by using a similar hydrothermal and calcination process. The detailed fabrication process of monolithic catalysts is presented in experimental section.

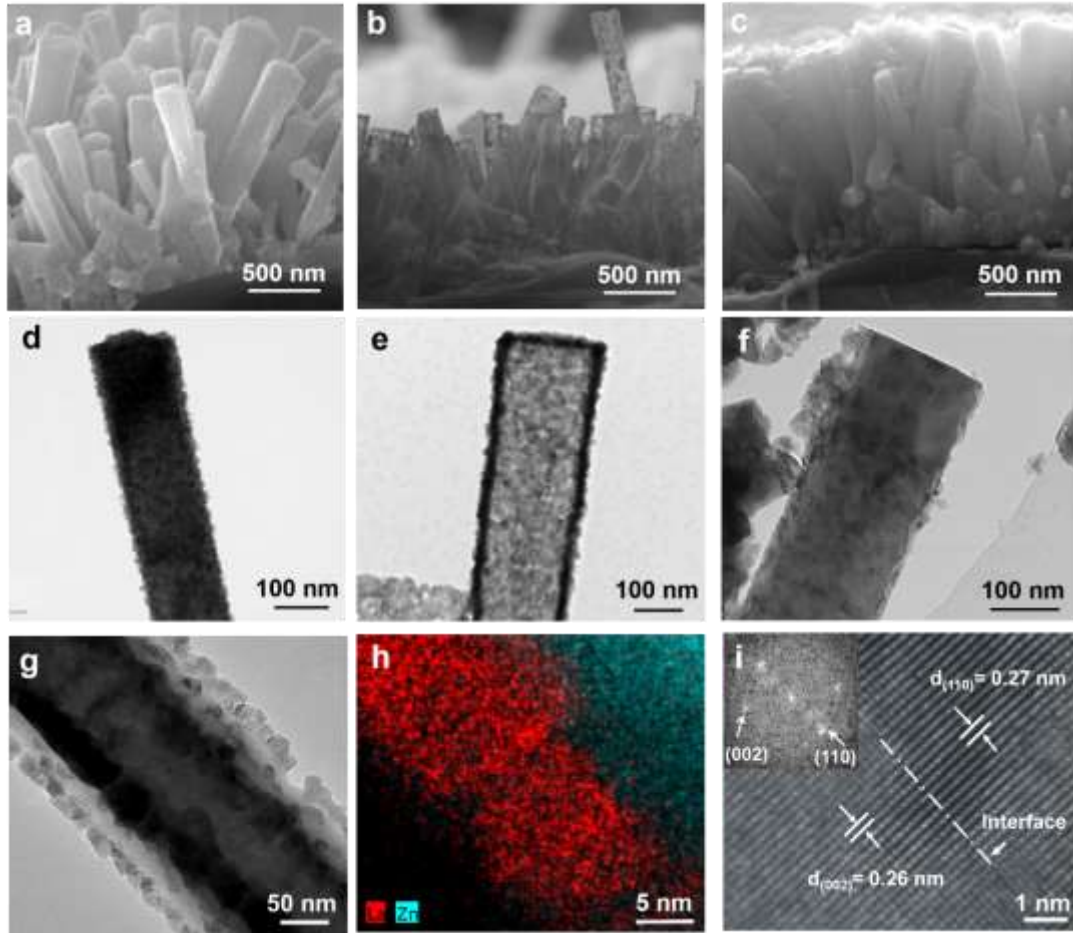


**Fig. 2.** SEM images of (a) ZnO/LSCO epitaxial heterojunction nanorod, (b) LSCO nanotube and (c) ZnO/SiO<sub>2</sub>/LSCO nanorod. TEM images of a typical (d) ZnO/LSCO epitaxial heterojunction nanorod, (e) LSCO nanotube and (f) ZnO/SiO<sub>2</sub>/LSCO nanorod. (g) STEM image of ZnO/LSCO epitaxial heterojunction nanorod. (h) EDX element mapping of La, Zn on the selected region of (g). (i) HRTEM image of ZnO/LSCO epitaxial interface and the corresponding FFT patterns.

Fig. 2 shows the morphology and microstructure characterization of the fabricated LSCO monolithic catalysts. Scanning electron microscope (SEM) images in Fig. 2a shows that ZnO/LSCO heterojunction nanorods are uniformly coated on honeycomb substrates, which is about 1  $\mu\text{m}$  in length and 100 to 300 nm in diameter. As shown in Fig. 2b, LSCO nanotube arrays retained the nano-array structure after reduction treatment and evenly distributed on the wall of honeycomb substrate with length of 1  $\mu\text{m}$  and diameter of 200 nm, which is consistent with the dimensionality of ZnO/LSCO

heterojunction nanorods. The LSCO nanotube structure also signifies ZnO nanorods (ZnO) could be effectively removed by H<sub>2</sub> reduction at elevated temperature. The SEM image of ZnO/SiO<sub>2</sub>/LSCO in Fig. 2c also exhibited regular nanorods array structure with the length of ca. 1 μm and the diameter of 150-200 nm. Figures 2d-2f presents transmission electron microscopy (TEM) images of typical single ZnO/LSCO heterojunction nanorod, LSCO nanotube and ZnO/SiO<sub>2</sub>/LSCO nanorod. Obviously, the hollow structure of LSCO nanotube (Figure 2e) intuitively showed the efficient removal of ZnO core, as well as the good uniformity of LSCO coating. While ZnO/LSCO and ZnO/SiO<sub>2</sub>/LSCO shows a solid rod-like structure. The XRD patterns in Figure S4 has further confirmed the purity of LSCO nanotube without the presence of ZnO, which proved H<sub>2</sub> reduction was an effective method for the preparation of LSCO nanotube monolithic catalysts. In addition, the inductively coupled plasma-atom emission spectrometer (ICP-AES) results (Table S1) proved that the amount of LSCO in both nano-array catalysts are identical.

As demonstrated by bright-field scanning transmission electron microscopy (STEM) in Fig. 2g, the ZnO/LSCO core-shell structure and the heterojunction interface can be easily observed from the higher magnification image of a typical ZnO/LSCO nanorod, where the LSCO nanoparticles of 0.5-20 nm in size dispersed on the ~150 nm wide ZnO nanorod surface. The elemental distribution boundary between La and Zn from Energy Dispersive X-Ray Spectroscopy (EDX) mapping in Fig. 2h further reveals the distinct interface. High resolution transmission electron microscopy (HRTEM) image (Fig. 2i) indicated that LSCO nanoparticles were epitaxially grown on ZnO {01-10} facets along the [110] direction, as evidenced by the measured lattice fringes of 0.26 nm and 0.27 nm matching to the {002} planes of ZnO and {110} planes in LSCO, respectively. The inset in Fig. 2i is the corresponding fast Fourier transformation (FFT), proving the coherent interface formed between ZnO and LSCO. In all, the experimental observations for constructed ZnO/LSCO model catalysts are in accordance with our theoretical predictions.

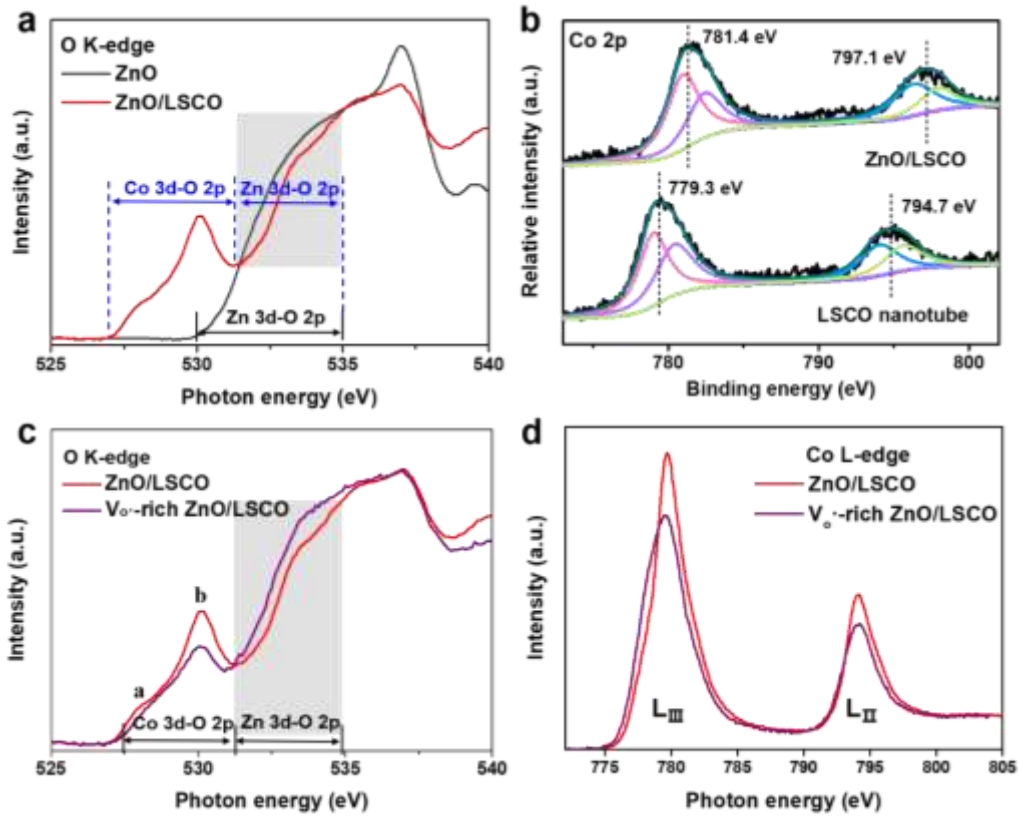


**Fig. 3.** (a) Normalized O K-edge XANES spectra of ZnO and ZnO/LSCO. (b) Co 2p, XPS spectra of ZnO/LSCO core-shell nanorod arrays and LSCO nanotube arrays. (c) Normalized O K-edge XANES spectra of ZnO/LSCO and  $V_{o\bullet}$ -rich ZnO/LSCO. (d) Normalized Co L-edge XANES spectra of ZnO/LSCO and  $V_{o\bullet}$ -rich ZnO/LSCO.

X-ray absorption near edge structure (XANES) is capable of studying electronic structure of surface/interface and thus was applied to gain experimental insight into the electron transfer between ZnO and LSCO (Fig. 3). To confirm the reversible electron transfer on ZnO/LSCO interface with  $V_{o\bullet}$ ,  $V_{o\bullet}$ -rich ZnO/LSCO was *in-situ* generated by Argon ion sputtering right after data collecting on pristine ZnO/LSCO sample in the XANES tests. The electronic structure change as well as charge transfer at both samples can be revealed by the spectra of O K edge ( $O 1s \rightarrow 2p$  transition) absorption. Fig. 3a shows the O K-edges XANES spectra of ZnO and ZnO/LSCO. Due to different hybridization energy between O  $2p$  and metal  $3d$  orbitals, we can divide the O near edge states into two main parts: (1) Co  $3d$ -O  $2p$  hybridization states ( $< 531.3$  eV), (2) Zn  $3d$ -O  $2p$  hybridization state ( $531.3 - 535.0$  eV). It is observed that the low energy Zn  $3d$ -O  $2p$  hybridization states are occupied and the whole spectrum (shaded area) has

shifted towards higher energy region, which indicates Zn 3d-O 2p hybridized orbital in the conduction band is occupied by electrons [49,50]. It signifies that ZnO would absorb/attract electron from LSCO upon the formation of ZnO/LSCO interface. Fig. 3b presents Co 2p XPS spectra of ZnO/LSCO epitaxial heterojunction and LSCO nanotube. The binding energy of Co 2p for ZnO/LSCO shifts positively compared to that of LSCO nanotube, indicating the increase of the Co valence state (lose electrons) in ZnO/LSCO and electron transfer between ZnO and LSCO, which is consistent with the results in Fig. 3a.

The O K-edge XANES spectra of ZnO/LSCO and  $V_{o\cdot}$ -rich ZnO/LSCO are shown in Fig. 3c, and the peaks labeled a and b are assigned to O 1s  $\rightarrow$  Co 3d-O 2p hybridized  $t_{2g}$  and  $e_g$  transition [51], respectively. On the contrary, it is clearly observed that the XANES spectrum of the Zn 3d-O 2p hybridization states (shaded area) presents a negative shift after  $V_{o\cdot}$  generation, indicating that the formation of rich  $V_{o\cdot}$  in ZnO/LSCO prompts the escape of electrons from Zn 3d-O 2p hybridized orbital [51]. More compelling, peak b presents significantly reduced intensity in  $V_{o\cdot}$  rich ZnO/LSCO, which suggests that Co 3d  $e_g$ -O 2p hybridized orbital in the conduction band is occupied by more electrons. Thereby, the electrons would be transferred from Zn 3d-O 2p hybrid orbital in ZnO to Co  $e_g$  orbital in LSCO after the generation of surface  $V_{o\cdot}$ . Co L-edge XANES spectra (Fig. 3d), that is sensitive to oxidation state and spin state, provide more detailed information of electron transfer on ZnO/LSCO interface. The Co  $L_{III}$ -edge shifts towards the lower energy region in the case of rich  $V_{o\cdot}$ , where surface Co ions exhibits a lower oxidation state due to electrons donation from ZnO to  $e_g$  orbital of Co in LSCO [52]. The XANES analysis of O K-edge and Co L-edge matches well with our DFT calculation.

### 3.3 Thermally catalytic performance of $CH_4$ oxidation

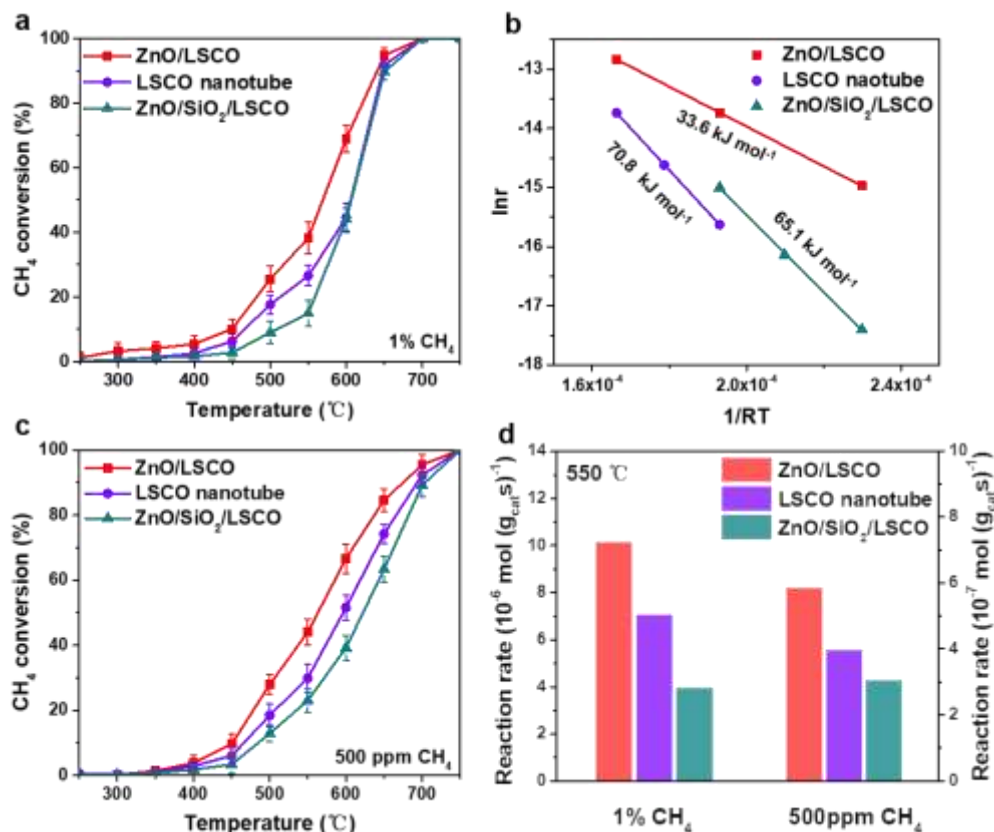


**Fig. 4.** (a) CH<sub>4</sub> conversion as a function of temperature over the ZnO/LSCO, LSCO nanotube and ZnO/SiO<sub>2</sub>/LSCO catalysts with the CH<sub>4</sub> concentration of 1%. (b) the corresponding Arrhenius plots for the reaction kinetics of CH<sub>4</sub> combustion of (a). (c) CH<sub>4</sub> conversion as a function of temperature over the ZnO/LSCO, LSCO nanotube and ZnO/SiO<sub>2</sub>/LSCO catalysts with the CH<sub>4</sub> concentration of 500 ppm. (d) The reaction rate of CH<sub>4</sub> oxidation under the CH<sub>4</sub> concentration of 1% and 500 ppm. (The weight hour space velocity (WHSV) is 200 L g<sup>-1</sup>h<sup>-1</sup> (~6000 h<sup>-1</sup> for gas hour space velocity (GHSV)) for all thermally catalytic methane oxidation tests)

In order to figure out the effect of ZnO/LSCO epitaxial interface on catalytic performance, activity of methane oxidation was evaluated on these monolithic catalysts (Fig. 4). The complete activity data is summarized in Table S2. To keep the surface chemical state consistent, ZnO/LSCO, LSCO nanotube and ZnO/SiO<sub>2</sub>/LSCO were first pretreated under 10% O<sub>2</sub> at 300 °C for 2h before performance tests [43].

Fig. 4a presented the light-off curves of CH<sub>4</sub> oxidation for these nano-array catalysts when the concentration of CH<sub>4</sub> is 1%. It can be observed that ZnO/LSCO

displays the best catalytic performance for methane combustion than other counterparts. The  $T_{50}$  (temperature of half conversion) value of ZnO/LSCO is 568 °C, 36 and 37 °C lower than that of LSCO nanotube (604 °C) and ZnO/SiO<sub>2</sub>/LSCO (605 °C), respectively. The corresponding Arrhenius plots in Fig. 4b also reveals that the calculated apparent activation energy ( $E_a$ ) of ZnO/LSCO (33.6 kJ mol<sup>-1</sup>) is much lower than that of LSCO nanotube (70.8 kJ mol<sup>-1</sup>) and ZnO/SiO<sub>2</sub>/LSCO (65.1 kJ mol<sup>-1</sup>), indicating its higher surface reactivity. Meanwhile when the concentration of CH<sub>4</sub> is 500 ppm (Fig. 4c), ZnO/LSCO still exhibited the highest catalytic activity ( $T_{50}$  = 562 °C) among all samples, which is 37 and 61 °C lower than that LSCO nanotube (599 °C) and ZnO/SiO<sub>2</sub>/LSCO (623 °C), respectively. Correlated with Fig. 4a and 4c, it is noted that ZnO/LSCO interface-promoted activity enhancement is more prominent at a lower CH<sub>4</sub> concentration. This is because that 1% CH<sub>4</sub> (a large amount of CH<sub>4</sub> molecule) may exceed oxidation capacity of interface-activated lattice oxygen limited by LSCO loadings on monolith. Fig. 4d depicts the associated reaction rate of tested nano-array catalysts. The highest reaction rate further confirmed superior surface reactivity of ZnO/LSCO.

The catalytic performance evaluation of NO and CO oxidation was then performed to further identify the interface-promoted effect. As shown in Figure S6 and S7, the test results also indicated the superior activity and robustness of ZnO/LSCO. It hints that ZnO/LSCO epitaxial interface plays an important role in the oxidation reactions. In addition, the N<sub>2</sub> adsorption-desorption isotherm and pore-size distributions (Figure S8, Table S3) of ZnO/LSCO and LSCO nanotube monolithic catalysts were characterized to investigate their textual properties. On one hand, ZnO/LSCO (18.5 nm) and LSCO nanotube (18.6 nm) displays the identical average pore diameter. The mesopores should come from the gaps of LSCO nanoparticles coated on ZnO nanorod. While on the other hand, the estimated surface area of LSCO nanotube (45 m<sup>2</sup>/g) is about twice of ZnO/LSCO (24 m<sup>2</sup>/g), which is due to the increased surface area from exposure of nanotube inner surface after removing the ZnO core. Nevertheless, higher surface area LSCO nanotubes (~45 m<sup>2</sup>g<sup>-1</sup>) exhibited inferior catalytic activity for CH<sub>4</sub> oxidation to

the ZnO/LSCO nanorods ( $24 \text{ m}^2\text{g}^{-1}$ ), further suggesting the well-designed epitaxial interface (Fig. 2g-2f) should account for the boosted activity in ZnO/LSCO sample compared to LSCO nanotube samples despite LSCO's superior redox activity [53].

### 3.4 Photothermal properties and performance

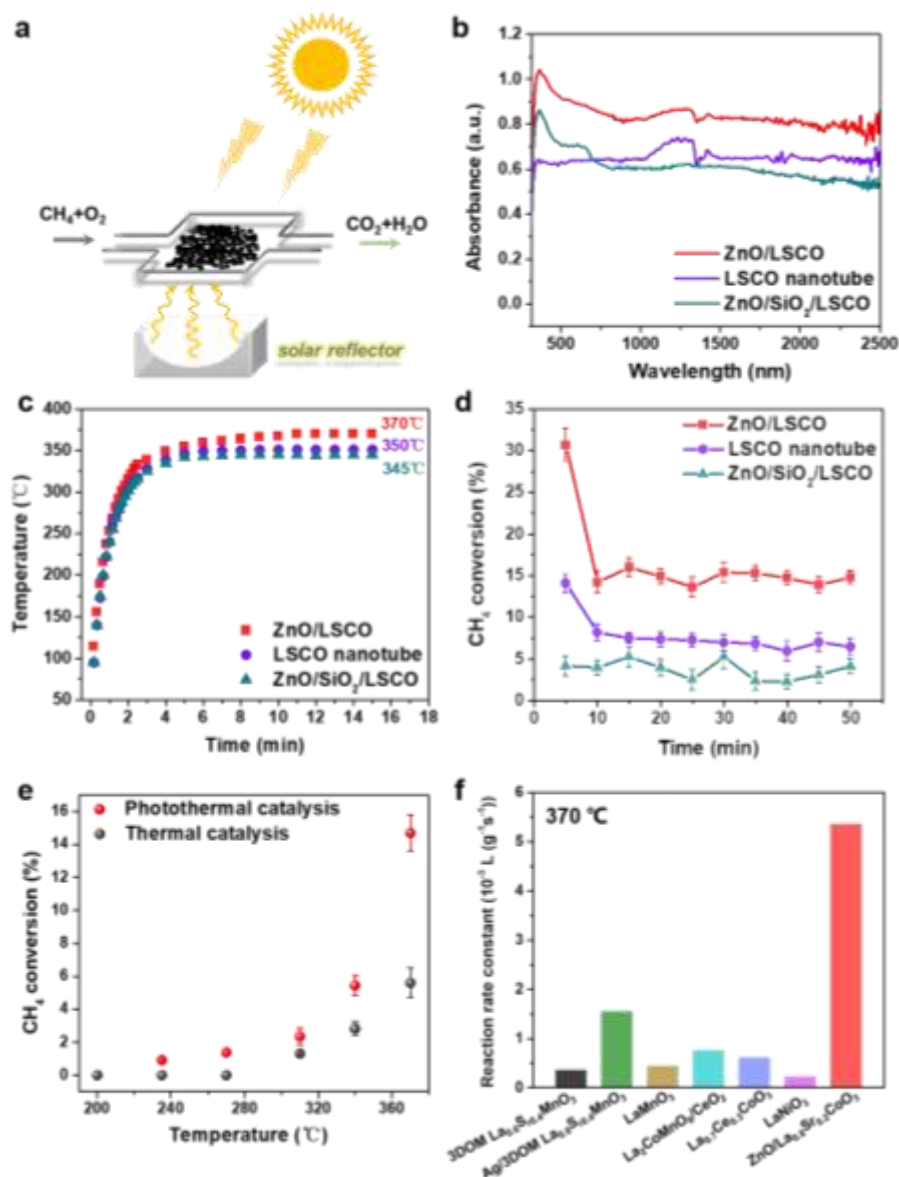


**Fig. 5.** (a) Scheme of photothermal catalytic reactor configuration. (b) UV-Vis-IR absorption spectra for the ZnO/LSCO, LSCO nanotube and ZnO/SiO<sub>2</sub>/LSCO catalysts. (c) Temperature profiles on these monolithic catalysts under the irradiation of the Xe lamp. (d) The CH<sub>4</sub> photothermal conversion over these monolithic catalysts under Xe lamp irradiation. (e) Comparison of CH<sub>4</sub> conversion for ZnO/LSCO under Xe lamp

irradiation and direct thermal heating (furnace) at the same temperature (The WHSV is ca.  $40 \text{ L g}^{-1}\text{h}^{-1}$  ( $1200 \text{ h}^{-1}$  for GHSV) for the part of photothermally catalytic methane oxidation and the corresponding thermal catalysis contrast). (f) Activity comparison of methane oxidation with previous studies by normalized reaction rate constant.

Inspired by the unique epitaxial interface and the potential photo/photo-thermal property of LSCO, we also explored the solar-driven catalysis of ZnO/LSCO for continuous-flow methane oxidation (Fig. 5). The novel solar reactor configuration is shown in Fig. 5a. The quartz device equipped with a solar reflector was specifically designed to meet the requirement of concentrated solar irradiation and to make full use of solar energy. CH<sub>4</sub> and O<sub>2</sub> are supplied to the flow-tube device under ambient pressure. Generally, the catalysts efficiently absorb solar radiation and simultaneously release the absorbed photons in the form of heat, thus increasing surface temperature and triggering catalytic reactions. The UV-Vis-IR diffuse reflectance spectra measurement was carried out to evaluate the optical response of ZnO/LSCO, LSCO nanotube and ZnO/SiO<sub>2</sub>/LSCO. Fig. 5b presented the absorption spectra of these catalysts. ZnO/LSCO exhibits the strongest light absorption across the whole region of solar spectrum, while LSCO nanotube and ZnO/SiO<sub>2</sub>/LSCO exhibit a slight decrease of absorbance. It suggests that the constructed epitaxial interface in ZnO/LSCO enables enhanced UV-Vis-IR response, which could be attributed to electronic interactions between ZnO and LSCO [54]. Compared with the absorption spectra of ZnO and ZnO/SiO<sub>2</sub> nanorods in Figure S9, the absorption band at 365 nm was assigned to an exciton transition of ZnO. And the wide band at the range of 540-651 nm should be assigned to the exciton absorption of La<sub>0.8</sub>Sr<sub>0.2</sub>CoO<sub>3</sub> [55]. While the bands at IR regions of ca. 1100-1400 nm were attributed to vibrations of surface carbonate species [56]. Then the temperature of the catalyst bed was monitored using a thermocouple in intimate contact with the surface of catalyst under Xe lamp irradiation. When the equilibrium is established between the absorption of solar and energy dissipation from the catalyst to the surroundings, the temperature would reach a plateau. As illustrated in Fig. 5c, the temperature of ZnO/LSCO, LSCO nanotube and ZnO/SiO<sub>2</sub>/LSCO

stabilizes at 370, 350 and 345 °C respectively after a rapid increase from room temperature in less than 6 min. Obviously, a stronger light adsorption on ZnO/LSCO results in a higher surface temperature, which would be partly favorable for highly efficient methane oxidation.

The solar-driven methane oxidation activity of these nano-array catalysts was evaluated under Xe lamp irradiation without any external heating. As shown in Fig. 5d, ZnO/LSCO exhibits remarkably increased activity for catalytic performance of methane oxidation, giving an average CH<sub>4</sub> conversion of 14.8 %, which is about 2 times of LSCO nanotube (7.10 %) and 4 times of ZnO/SiO<sub>2</sub>/LSCO (3.64%), indicating ZnO/LSCO epitaxial interface plays an important role in solar-driven catalysis. Besides, ZnO/LSCO, LSCO nanotube and ZnO/SiO<sub>2</sub>/LSCO exhibited excellent photothermal stability with stable conversion efficiency during five cycles of CH<sub>4</sub>-oxidation tests (Figure S10), indicating the promising potential for practical industrial application. The XRD and XPS results (Figure S11 and S12, Table S5) of fresh and spent LSCO monolithic catalysts also suggest their high surface structure and chemical stability. Fig. 5e presents the comparison of CH<sub>4</sub> conversion for ZnO/LSCO under photothermal heating (Xe lamp irradiation) and direct thermal heating (furnace). ZnO/LSCO presents 2.35, 5.43 and 14.7% CH<sub>4</sub> conversion in solar-driven system at 310, 340 and 370 °C, respectively, which is correspondingly about 1.8, 1.9 and 2.6 times higher than the thermal catalysis system (1.31, 2.82 and 5.60%), directly highlighting the further promotion effect of solar-driven catalysis. The synergy of photothermal and photocatalytic effect under solar illumination would result in ~2 times higher methane oxidation activity than thermal catalysis. Besides, the photothermally catalytic performance of ZnO/LSCO is compared with other reported platinum group metal free perovskite catalysts by normalized reaction rate constant, as show in Fig. 5f [57–62]. ZnO/LSCO exhibits >3.5 times higher reaction rate constant than other perovskite, indicating a much higher methane oxidation activity and thus highlighting high efficiency of solar-driven CH<sub>4</sub> oxidation.

### *3.5 Catalytic mechanism elucidation*

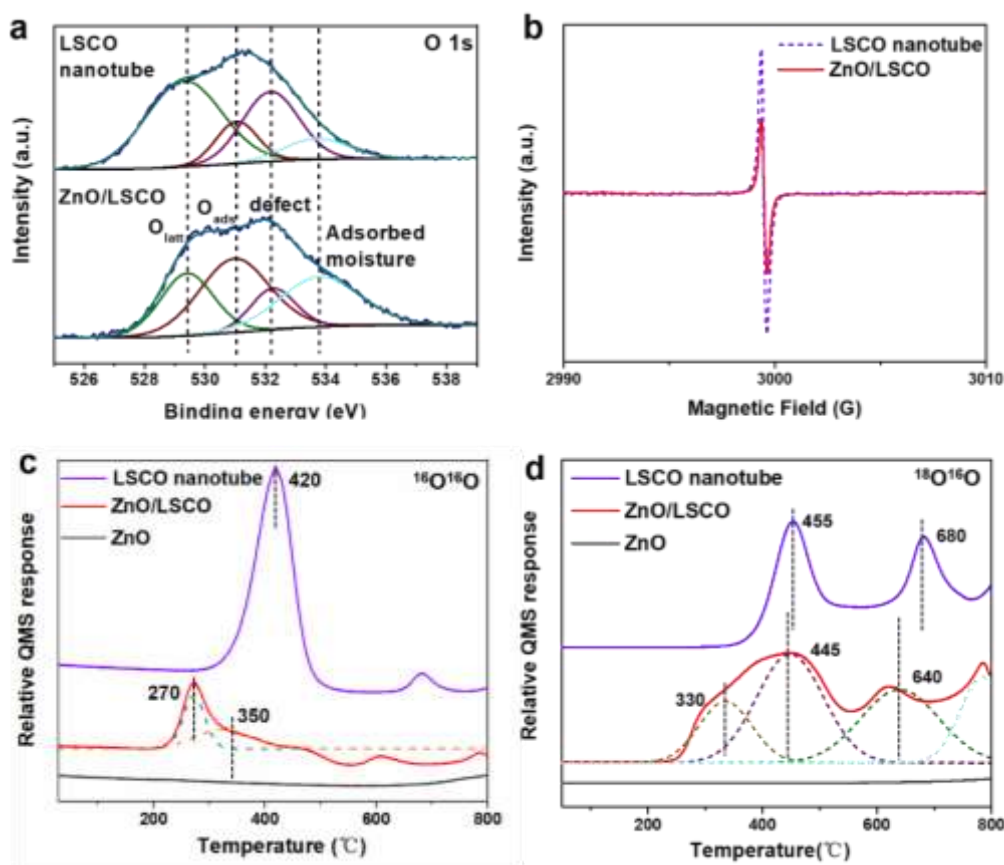


**Fig. 6.** (a) O 1s XPS spectra of ZnO/LSCO and LSCO nanotube. (b) Low-temperature EPR spectra of ZnO/LSCO and LSCO.  $O_{\text{lat}}$  mobility study by  $^{18}\text{O}$ -TPD: QMS profiles of (c)  $^{16}\text{O}^{16}\text{O}$  and (d)  $^{18}\text{O}^{16}\text{O}$ , during oxygen isotopic exchange over ZnO/LSCO, LSCO nanotube and ZnO nanorod based on same sample weight.

To disclose the relationship between the electron transfer on ZnO/LSCO interface and methane catalytic activity, the carbon monoxide temperature programmed reduction (CO-TPR) profiles (Figure S13) of ZnO/LSCO and LSCO nanotube nanoarray catalysts were firstly investigated. Generally speaking, the reduction process of cobalt oxide could be divided into two sections: (1)  $\text{Co}^{3+} \rightarrow \text{Co}^{2+}$  and (2)  $\text{Co}^{2+} \rightarrow \text{Co}^0$ . [63–65] In the case of ZnO/LSCO, there are four main reduction peaks at 330  $^{\circ}\text{C}$ , 550  $^{\circ}\text{C}$ , 680  $^{\circ}\text{C}$  and 780  $^{\circ}\text{C}$ . The first two reduction peaks at 330  $^{\circ}\text{C}$ , 550  $^{\circ}\text{C}$  could be attributed to reduction of  $\text{Co}^{3+}$ ,  $\text{Co}^{2+}$ , respectively. For LSCO nanotube, the corresponding reduction peaks shift positively to 425 and 555  $^{\circ}\text{C}$ . In addition, the other reduction peaks centered at 680  $^{\circ}\text{C}$  and 770  $^{\circ}\text{C}$  for ZnO/LSCO should be ascribed to

the reduction of ZnO observed from ZnO reduction spectrum [42]. On the other hand, for both samples, surface  $O_{\text{latt}}$  bonds with cobalt ions, through  $\text{Co}^{3+}-\text{O}^{2-}$  and  $\text{Co}^{2+}-\text{O}^{2-}$  [66], and the reduction reactions require breaking of the  $O_{\text{latt}}$  bonds. Therefore, the fact that ZnO/LSCO displays a reduction peak at a much lower temperature (330 °C) than that of LSCO nanotube (425 °C) suggests the better low-temperature reducibility and more active surface  $O_{\text{latt}}$  [67]. The active surface  $O_{\text{latt}}$  would be directly responsible for its high  $\text{CH}_4$  catalytic activity [65].

Besides, the higher reactivity of  $O_{\text{latt}}$  is also conducive to the rapid transformation (formation and refill) of oxygen vacancy ( $V_{\text{o}}\cdot$ ) [68]. Surface oxygen vacancy and its role in surface reactivity was then systematically investigated (Fig. 6). X-ray Photoelectron Spectroscopy (XPS) [69] was applied to identify surface valence states and defects on nano-array catalysts. The broad XPS O 1s peak of ZnO/LSCO and LSCO nanotube (Fig. 6a) could be deconvoluted into four major components, including adsorbed moisture, oxygen defect ( $V_{\text{o}}\cdot$ ), surface adsorbed oxygen ( $O_{\text{ads}}$ :  $\text{O}_2^-$ ,  $\text{O}_2^{2-}$ ,  $\text{O}^-$ ) and  $O_{\text{latt}}$  [70]. According to quantitative analysis, the  $O_{\text{ads}}/O_{\text{latt}}$  molar ratio of ZnO/LSCO (1.545) is about 5 times higher than that of LSCO nanotube (0.268), indicating a greater amount of surface adsorbed oxygen on ZnO/LSCO surface. While it is worth noting that  $V_{\text{o}}\cdot/O_{\text{latt}}$  ratio of ZnO/LSCO (0.556) is lower than that of LSCO nanotube (0.600). Furthermore, low-temperature electron paramagnetic resonance (EPR) analysis (Fig. 6b) shows that the  $V_{\text{o}}\cdot$  ( $g = 2.001$ ) [71] concentration in LSCO nanotube is higher than that in ZnO/LSCO. Considering the oxygen rich atmosphere in both our activity evaluation condition (1%/500 ppm  $\text{CH}_4$ , 20%  $\text{O}_2$ ,  $\text{N}_2$  balance) and the practical industrial application (ventilation air: ~21%  $\text{O}_2$ ) [72], the lower concentration of  $V_{\text{o}}\cdot$  detected in ZnO/LSCO may be related to the surface  $O_{\text{latt}}$  mobility in ZnO/LSCO, which bilaterally facilitates the rapid refilling of  $V_{\text{o}}\cdot$  by  $O_{\text{ads}}$ .

To test the assumption, isotope labeling  $^{18}\text{O}$  Temperature Programed Desorption ( $^{18}\text{O}$ -TPD) experiment was carried out to examine the mobility of  $O_{\text{latt}}$  in these nano-array catalysts. Since  $^{18}\text{O}_2$  is the only oxygen species in the atmosphere during the TPD process, all released  $^{16}\text{O}^{16}\text{O}$  originates from the chemically adsorbed  $O_{\text{ads}}$  and  $O_{\text{latt}}$  of

testing catalysts, and the  $^{18}\text{O}^{16}\text{O}$  detected will be from the surface  $\text{O}_{\text{latt}}$  of  $^{18}\text{O}/^{16}\text{O}$  (lattice) in the testing catalysts which formed due to the migrating of  $^{18}\text{O}$  from atmosphere to catalysts surface. From Fig. 6c, the broad  $^{16}\text{O}^{16}\text{O}$  desorption peak from around 200 to 400 °C in ZnO/LSCO can be deconvoluted and ascribed to  $\text{O}_{\text{ads}}$  and surface  $\text{O}_{\text{latt}}$  desorption peaks centered at 270 and 350 °C, respectively [66]. A broad low temperature  $^{18}\text{O}^{16}\text{O}$  desorption peaks peak for ZnO/LSCO in Fig. 6d could also be deconvoluted into three major desorption peaks at 330, 445 and 640 °C, attributable to desorption of surface  $\text{O}_{\text{latt}}$ , sub-surface  $\text{O}_{\text{latt}}$  and bulk  $\text{O}_{\text{latt}}$ , respectively [68]. While for LSCO nanotube, surface  $\text{O}_{\text{latt}}$  and bulk  $\text{O}_{\text{latt}}$  release at higher temperature, and there is almost no  $\text{O}_{\text{ads}}$ . It is widely accepted that the lower the isotopomer evolution temperature is, the higher is the  $\text{O}_{\text{latt}}$  mobility and reactivity [67,70]. Thereby, ZnO/LSCO has higher  $\text{O}_{\text{latt}}$  mobility and enhanced  $\text{O}_{\text{latt}}$  reactivity than LSCO nanotube. According to quantitative analysis, the ratio of  $^{18}\text{O}^{16}\text{O}/^{16}\text{O}^{16}\text{O}$  from surface  $\text{O}_{\text{latt}}$  desorption in ZnO/LSCO is 34.8, which indicates there existed high-reactivity sites on the ZnO/LSCO surface for the benefit of the rapid transformation of  $^{18}\text{O}_{\text{ads}}$  from  $^{18}\text{O}^{18}\text{O}$  atmosphere to surface  $\text{O}_{\text{latt}}$ . The large amount of desorbed  $^{16}\text{O}^{16}\text{O}$  (centered at 270 °C) should be due to the rapid transformation of a portion of surface  $\text{O}_{\text{latt}}$  to  $\text{O}_{\text{ads}}$ , which has further confirmed the high exchange rate between  $\text{O}_{\text{ads}}$  and surface  $\text{O}_{\text{latt}}$ . For LSCO nanotube, either the poor adsorbed oxygen capacity or inferior transformation ability of  $\text{O}_{\text{latt}}$  has led to very small amount of desorbed  $\text{O}_{\text{ads}}$ . Correlated with DFT calculation and XANES results, it is interpreted that on the ZnO/LSCO interface, the shift of electron cloud density deviating from Co to ZnO will activate the  $\text{O}_{\text{latt}}$  in LSCO by weakening the strength of covalent bond between O and Co. The  $\text{O}_{\text{latt}}$  in LSCO is activated and reacts with adsorbed  $\text{CH}_4$  molecular via Mars and van Krevelen (MvK) mechanism [48], which would generate  $\text{V}_{\text{o}}\cdot$  as return; Once  $\text{V}_{\text{o}}\cdot$  are generated, ZnO, as electrons donor, would in turn transfer electron to the  $e_g$  orbital of Co atoms and promote the regeneration of  $\text{O}_{\text{latt}}$  from  $\text{O}_{\text{ads}}$ . in LSCO for the following  $\text{CH}_4$  oxidation round. This should account for the superior  $\text{O}_{\text{latt}}$  reactivity and mobility, and thus easier mutual transformation between  $\text{O}_{\text{latt}}$  and  $\text{O}_{\text{ads}}$  in ZnO/LSCO.

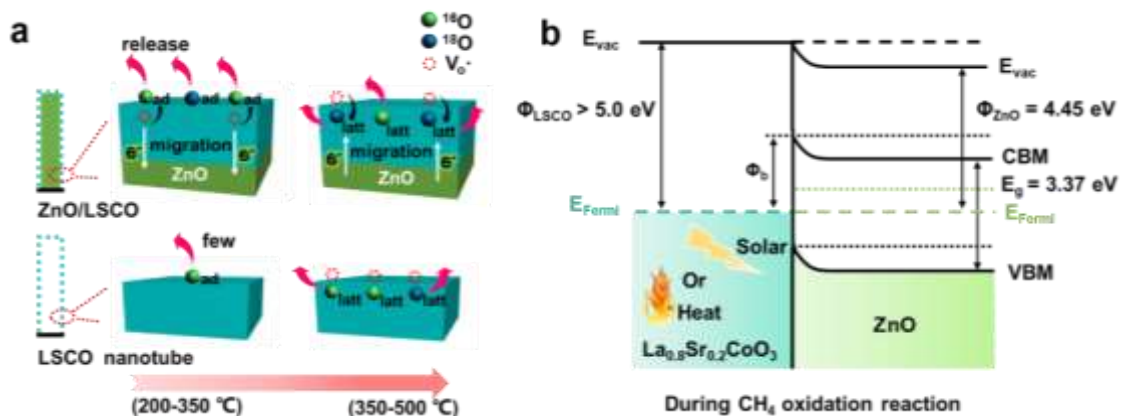


**Fig. 7.** (a) Schematic summary of  $\text{O}_{\text{latt}}$  migration and transformation in the process of  $^{18}\text{O}$ -TPD (“ad” denoted as  $\text{O}_{\text{ads}}$ , “latt” denoted as  $\text{O}_{\text{latt}}$ ). (b) Schematic energy band structure alignment of ZnO/LSCO hetero-interface during reaction (Schottky junction) [55,73,74]. ( $\Phi_{\text{LSCO}}$ ,  $\Phi_{\text{ZnO}}$  is the work function of LSCO and ZnO, respectively.  $\Phi_{\text{b}}$  is the Schottky barrier height.  $E_{\text{g}}$  and  $E_{\text{F}}$  and  $E_{\text{vac}}$  referred to band gap, Fermi energy level and vacuum level, respectively. CBM and VBM refers to conduction band minimum and valence band maximum, respectively).

As shown in Fig. 7a, a schematic diagram was illustrated to better understand  $\text{O}_{\text{latt}}$  migration and transformation in the process of  $^{18}\text{O}$ -TPD. The efficient migration of surface  $\text{O}_{\text{latt}}$  with electron gain or loss in ZnO/LSCO promotes the fast formation and transformation (refilling of  $\text{O}_{\text{latt}}$ ) of  $\text{V}_{\text{o}}\cdot$ , which accounts for the lower concentration nature of  $\text{V}_{\text{o}}\cdot$  observed in ZnO/LSCO. To further verify this explanation, the formation energies of  $\text{V}_{\text{o}}\cdot$  for ZnO/LSCO (interface) and LSCO nanotube (surface) models were calculated as presented in Figure S14. It shows that the  $\text{V}_{\text{o}}\cdot$  formation energy on ZnO/LSCO surface was  $\sim 0.25 \text{ eV}$  lower than that on the pure LSCO, which suggests that  $\text{V}_{\text{o}}\cdot$  favorably forms on ZnO/LSCO surface and confirms there is highly active  $\text{O}_{\text{latt}}$  in ZnO/LSCO. Therefore, the engineered ZnO/LSCO epitaxial interface can function as an “electron regulator” to significantly adjust the reversible electron transfer, leading to exceptional boost of high-activity and high-mobility  $\text{O}_{\text{latt}}$ .

We also accounted for the origin of enhanced activity driven by solar energy. Owing to characteristic properties of LSCO from a  $p$ -type semiconductor state with an

narrow energy gap at room temperature to metallic-like state with no energy gap at  $>200\text{ }^{\circ}\text{C}$  [55], there is a transition from ZnO/LSCO heterojunction to ZnO/LSCO Schottky junction once the temperature is higher than  $200\text{ }^{\circ}\text{C}$  (Fig. 7b) [75]. With efficient electron transfer regulated by thermal effect, solar light simultaneously excites electrons of metallic state LSCO and then promote rapid electrons transfer from LSCO to ZnO through epitaxial interface, which further accelerates reversible electron transfer between ZnO and LSCO. Thus in our solar-driven catalytic system, the synergy of photothermal effect and photocatalytic effect may jointly facilitate the reversible charge transfer, which is superior to a single thermal-drive system. Solar irradiation induced formation of high-activity hole-trapped lattice oxygen ( $\text{O}^{2-}$ ) on oxide catalyst surface was also reported [76,77]. Above these further boosts the generation of high-activity and high-mobility  $\text{O}_{\text{latt}}$ . Therefore, both photothermal-activated  $\text{O}_{\text{latt}}$  and photo-activated  $\text{O}_{\text{latt}}$  reacts with adsorbed  $\text{CH}_4$  molecular via Mars and van Krevelen (MvK) mechanism [48], together facilitating  $\text{CH}_4$  oxidation process by a combination of photothermal and photoelectric effect.

#### 4. Conclusions

In conclusion, the feasibility of a solar driven catalytic strategy for methane oxidation has been demonstrated under high velocity continuous flow, and the epitaxial interface in  $\text{ZnO}/\text{La}_{0.8}\text{Sr}_{0.2}\text{CoO}_3$  (ZnO/LSCO) as a unique “electron regulator” has been identified to significantly boost the charge transfer and surface lattice oxygen activity during the catalytic methane oxidation. Through coherent ZnO/LSCO interfaces, efficient and reversible electron transfer between Zn  $3d$ -O  $2p$  hybrid orbital in ZnO and Co  $e_g$  orbital in LSCO promotes the lattice oxygen species activity as well as the fast formation and transformation of oxygen vacancies, and enhances surface reactivity greatly. The synergetic drive of photothermal and photoelectric effects further facilitates reversible charge transfer, which leads to higher lattice oxygen activity and thus better solar-driven  $\text{CH}_4$  oxidation activity. The solar-driven methane catalytic oxidation strategy provides a promising pathway for emitted methane utilization in variou mobile and stationary energy generation and petrochemical plants, and epitaxial

interface design concept provides a new approach for the design and fabrication of efficient PGM free oxidation catalysts.

## **Acknowledgements**

Ji Yang and Wen Xiao contribute equally to this work. The authors are grateful for the financial support from the National Natural Science Foundation of China (No. 21777051), The Recruitment Program of Global Young Experts start-up funds, The Program of Introducing Talents of Discipline to Universities of China (111 program, B17019), the U.S. Department of Energy (DOE) (Award Nos. DE-EE0000210 and DE-EE0006854) and the U.S. National Science Foundation (Award No. CBET 1344792). Z. W. was supported by the U.S. DOE Office of Science, Office of Basic Energy Sciences, Chemical Sciences, Geosciences, and Biosciences Division. Part of the work including CO-TPR and O<sub>2</sub> isotope exchange experiments were conducted at the Center for Nanophase Materials Sciences at the Oak Ridge National Laboratory, a DOE Office of Science User Facility. The authors would like to acknowledge the Singapore Synchrotron Light Source (SSLS) for providing the facility necessary for conducting the research. The Laboratory is a National Research Infrastructure under the National Research Foundation Singapore.

## **Appendix A. Supplementary data**

Supplementary material related to this article can be found, in the online version.

## **References**

- [1] J. Xie, R. Jin, A. Li, Y. Bi, Q. Ruan, Y. Deng, Y. Zhang, S. Yao, G. Sankar, D. Ma, J. Tang, Highly selective oxidation of methane to methanol at ambient conditions by titanium dioxide-supported iron species, *Nat. Catal.* 1 (2018) 889–896. <https://doi.org/10.1038/s41929-018-0170-x>.
- [2] Zubin Bamji and Francisco Sucre, An international partnership: The "Zero Routine Flaring by 2030" Initiative, presented at Inauguration of Minster's Meeting, OLADE Energy Week, Buenos Aires, December 2017.
- [3] The World Bank, Global gas flaring reduction partnership (GGFR)-Gas flaring

- data 2013-2017, <http://www.worldbank.org/en/programs/gasflaringreduction>, 2018 (accessed: December 2018).
- [4] E.G. Nisbet, P. Dlugokencky, Edward J. Bousquet, Methane on the rise—again, *Science* 343 (2014) 493–495. <https://doi.org/10.1126/science.1247828>.
- [5] A.W. Petrov, D. Ferri, F. Krumeich, M. Nachttegaal, J.A. Van Bokhoven, O. Kröcher, Stable complete methane oxidation over palladium based zeolite catalysts, *Nat. Commun.* 9 (2018) 2545. <https://doi.org/10.1038/s41467-018-04748-x>.
- [6] Y. Wang, H. Arandiyani, H.A. Tahini, J. Scott, X. Tan, H. Dai, J.D. Gale, A.L. Rohl, S.C. Smith, R. Amal, The controlled disassembly of mesostructured perovskites as an avenue to fabricating high performance nanohybrid catalysts, *Nat. Commun.* 8 (2017) 15553. <https://doi.org/10.1038/ncomms15553>.
- [7] A. Hu, J.J. Guo, H. Pan, Z. Zuo, Selective functionalization of methane, ethane, and higher alkanes by cerium photocatalysis, *Science* 361 (2018) 668–672. <https://doi.org/10.1126/science.aat9750>.
- [8] X. Chen, Y. Li, X. Pan, D. Cortie, X. Huang, Z. Yi, Photocatalytic oxidation of methane over silver decorated zinc oxide nanocatalysts, *Nat. Commun.* 7 (2016) 12273. <https://doi.org/10.1038/ncomms12273>.
- [9] H. Zhang, P. Zhang, M. Qiu, J. Dong, Y. Zhang, X.W. (David) Lou, Ultrasmall MoO<sub>x</sub> Clusters as a Novel Cocatalyst for Photocatalytic Hydrogen Evolution, *Adv. Mater.* 31 (2019) 1804883. <https://doi.org/10.1002/adma.201804883>.
- [10] H. Zhang, G. Liu, L. Shi, H. Liu, T. Wang, J. Ye, Engineering coordination polymers for photocatalysis, *Nano Energy* 22 (2016) 149–168. <https://doi.org/10.1016/j.nanoen.2016.01.029>.
- [11] H. Zhang, J. Nai, L. Yu, X.W. (David) Lou, Metal-Organic-Framework-Based Materials as Platforms for Renewable Energy and Environmental Applications, *Joule* 1 (2017) 77–107. <https://doi.org/10.1016/j.joule.2017.08.008>.
- [12] H. Zhang, J. Wei, J. Dong, G. Liu, L. Shi, P. An, G. Zhao, J. Kong, X. Wang, X. Meng, J. Zhang, J. Ye, Efficient Visible-Light-Driven Carbon Dioxide

- Reduction by a Single-Atom Implanted Metal–Organic Framework, *Angew. Chem. Int. Ed.* 55 (2016) 14310–14314. <https://doi.org/10.1002/anie.201608597>.
- [13] J. Yang, D. Wang, H. Han, C. Li, Roles of cocatalysts in photocatalysis and photoelectrocatalysis, *Acc. Chem. Res.* 46 (2013) 1900–1909. <https://doi.org/10.1021/ar300227e>.
- [14] Y. Zhao, W. Gao, S. Li, G.R. Williams, A.H. Mahadi, D. Ma, Solar- versus Thermal-Driven Catalysis for Energy Conversion, *Joule* 3 (2019) 1–18. <https://doi.org/10.1016/j.joule.2019.03.003>.
- [15] J. Schneider, M. Matsuoka, M. Takeuchi, J. Zhang, Y. Horiuchi, M. Anpo, D.W. Bahnemann, Understanding TiO<sub>2</sub> Photocatalysis: Mechanisms and Materials, *Chem. Rev.* 114 (2014) 9919–9986. <https://doi.org/doi.org/10.1021/cr5001892>.
- [16] J.J. Li, E.Q. Yu, S.C. Cai, X. Chen, J. Chen, H.P. Jia, Y.J. Xu, Noble metal free, CeO<sub>2</sub>/LaMnO<sub>3</sub> hybrid achieving efficient photo-thermal catalytic decomposition of volatile organic compounds under IR light, *Appl. Catal. B Environ.* 240 (2019) 141–152. <https://doi.org/10.1016/j.apcatb.2018.08.069>.
- [17] Z. Li, J. Liu, Y. Zhao, G.I.N. Waterhouse, G. Chen, R. Shi, X. Zhang, X. Liu, Y. Wei, X.D. Wen, L.Z. Wu, C.H. Tung, T. Zhang, Co-based catalysts derived from layered-double-hydroxide nanosheets for the photothermal production of light olefins, *Adv. Mater.* 30 (2018) 1800527. <https://doi.org/10.1002/adma.201800527>.
- [18] H. Zhang, T. Wang, J. Wang, H. Liu, T.D. Dao, M. Li, G. Liu, X. Meng, K. Chang, L. Shi, T. Nagao, J. Ye, Surface-Plasmon-Enhanced Photodriven CO<sub>2</sub> Reduction Catalyzed by Metal-Organic-Framework-Derived Iron Nanoparticles Encapsulated by Ultrathin Carbon Layers, *Adv. Mater.* 28 (2016) 3703–3710. <https://doi.org/10.1002/adma.201505187>.
- [19] G. Chen, R. Gao, Y. Zhao, Z. Li, G.I.N. Waterhouse, R. Shi, J. Zhao, M. Zhang, L. Shang, G. Sheng, X. Zhang, X. Wen, L.Z. Wu, C.H. Tung, T. Zhang, Alumina-supported CoFe alloy catalysts derived from layered-double-hydroxide nanosheets for efficient photothermal CO<sub>2</sub> hydrogenation to hydrocarbons, *Adv.*

- Mater. 30 (2018) 1704663. <https://doi.org/10.1002/adma.201704663>.
- [20] Y. Ma, Y. Li, M. Mao, J. Hou, M. Zeng, X. Zhao, Synergetic effect between photocatalysis on TiO<sub>2</sub> and solar light-driven thermocatalysis on MnO<sub>x</sub> for benzene purification on MnO<sub>x</sub>/TiO<sub>2</sub> nanocomposites, *J. Mater. Chem. A* 3 (2015) 5509–5516. <https://doi.org/10.1039/c5ta00126a>.
- [21] M. Zeng, Y. Li, M. Mao, J. Bai, L. Ren, X. Zhao, Synergetic effect between photocatalysis on TiO<sub>2</sub> and thermocatalysis on CeO<sub>2</sub> for gas-phase oxidation of benzene on TiO<sub>2</sub>/CeO<sub>2</sub> nanocomposites, *ACS Catal.* 5 (2015) 3278–3286. <https://doi.org/10.1021/acscatal.5b00292>.
- [22] M. Zhu, M. Fujitsuka, L. Zeng, M. Liu, T. Majima, Dual function of graphene oxide for assisted exfoliation of black phosphorus and electron shuttle in promoting visible and near-infrared photocatalytic H<sub>2</sub> evolution, *Appl. Catal. B Environ.* 256 (2019) 117864. <https://doi.org/10.1016/j.apcatb.2019.117864>.
- [23] C. Zhai, M. Sun, L. Zeng, M. Xue, J. Pan, Y. Du, M. Zhu, Construction of Pt/graphitic C<sub>3</sub>N<sub>4</sub>/MoS<sub>2</sub> heterostructures on photo-enhanced electrocatalytic oxidation of small organic molecules, *Appl. Catal. B Environ.* 243 (2019) 283–293. <https://doi.org/10.1016/j.apcatb.2018.10.047>.
- [24] M. Behrens, F. Studt, I. Kasatkin, S. Kühn, M. Hävecker, F. Abild-pedersen, S. Zander, F. Girgsdies, P. Kurr, B. Kniep, M. Tovar, R.W. Fischer, J.K. Nørskov, R. Schlögl, The Active Site of Methanol Synthesis over Cu/ZnO/Al<sub>2</sub>O<sub>3</sub> Industrial Catalysts, *Science* 336 (2012) 893–898. <https://doi.org/10.1126/science.1219831>.
- [25] S.T. Hunt, M. Milina, A.C. Alba-Rubio, C.H. Hendon, J.A. Dumesic, Y. Román-Leshkov, Self-assembly of noble metal monolayers on transition metal carbide nanoparticle catalysts, *Science* 352 (2016) 974–978. <https://doi.org/10.1126/science.aad8471>.
- [26] S. Chen, S. Shen, G. Liu, Y. Qi, F. Zhang, C. Li, Interface engineering of a CoO<sub>x</sub>/Ta<sub>3</sub>N<sub>5</sub> photocatalyst for unprecedented water oxidation performance under visible-light-irradiation, *Angew. Chem. Int. Ed.* 54 (2015) 3047–3051.

- <https://doi.org/10.1002/anie.201409906>.
- [27] C.H. Cui, S.H. Yu, Engineering interface and surface of noble metal nanoparticle nanotubes toward enhanced catalytic activity for fuel cell applications, *Acc. Chem. Res.* 46 (2013) 1427–1437. <https://doi.org/10.1021/ar300254b>.
- [28] J. Yang, Y. Guo, Nanostructured perovskite oxides as promising substitutes of noble metals catalysts for catalytic combustion of methane, *Chin. Chem. Lett.* 29 (2018) 252–260. <https://doi.org/10.1016/j.ccllet.2017.09.013>.
- [29] S. Royer, D. Duprez, F. Can, X. Courtois, C. Batiot-dupeyrat, S. Laassiri, H. Alamdari, Perovskites as substitutes of noble metals for heterogeneous catalysis: Dream or reality, *Chem. Rev.* 114 (2014) 10292–10368. <https://doi.org/10.1021/cr500032a>.
- [30] J. Li, E. Yu, S. Cai, X. Chen, J. Chen, H. Jia, Noble metal free, CeO<sub>2</sub>/LaMnO<sub>3</sub> hybrid achieving efficient photo-thermal catalytic decomposition of volatile organic compounds under IR light, *Appl. Catal. B Environ.* 240 (2019) 141–152. <https://doi.org/10.1016/j.apcatb.2018.08.069>.
- [31] A.M. Loshkareva, N. N., Sukhorukov, Y. P., Mostovshchikova, E. V., Nomerovannaya, L. V., Makhnev, A. A., Naumov, S. V., Gan'shina, E. A., Rodin, I. K., Moskvin, A. S., and Balbashov, The evolution of the optical spectra of LaMnO<sub>3</sub> under light n- and p-Type doping and the separation of phases, *J. Exp. Theor. Phys.* 94 (2002) 350–355. <https://doi.org/10.1134/1.1458485>.
- [32] V.S. Wierschem, M., Kapphan, S., and Vikhnin, IR absorption of trapped and free Jahn–Teller polarons in 3D-crystals and films of LaMnO<sub>3</sub> and La<sub>2/3</sub>Sr<sub>1/3</sub>MnO<sub>3</sub>, *Ferroelectrics* 1 (2004) 49–54. <https://doi.org/10.1080/00150190490428700>.
- [33] G. Kresse, J. Furthmüller, Efficient iterative schemes for ab initio total-energy calculations using a plane-wave basis set, *Phys. Rev. B* 54 (1996) 11169. <https://doi.org/10.1103/PhysRevB.54.11169>.
- [34] P.E. Blöchl, Projector augmented-wave method, *Phys. Rev. B* 50 (1994) 17953. <https://doi.org/10.1103/PhysRevB.50.17953>.

- [35] J.P. Perdew, J. Chevary, S. Vosko, K. Jackson, M. Pederson, D. Singh, C. Fiolhais, Atoms, molecules, solids, and surfaces: Applications of the generalized gradient approximation for exchange and correlation, *Phys. Rev. B* 46 (1992) 6671. <https://doi.org/10.1103/PhysRevB.46.6671>.
- [36] J.P. Perdew, K. Burke, M. Ernzerhof, Generalized Gradient Approximation Made Simple, *Phys. Rev. Lett.* 77 (1996) 3865. <https://doi.org/10.1103/PhysRevLett.77.3865>.
- [37] J.D. Pack, H.J. Monkhorst, Special points for Brillouin-zone integrations, *Phys. Rev. B* 13 (1976) 5188. <https://doi.org/10.1103/PhysRevB.13.5188>.
- [38] J. Yang, S. Hu, Y. Fang, S. Hoang, L. Li, W. Yang, Z. Liang, J. Wu, J. Hu, W. Xiao, C. Pan, Z. Luo, J. Ding, L. Zhang, Y. Guo, Oxygen Vacancy Promoted O<sub>2</sub> Activation over Perovskite Oxide for Low-Temperature CO Oxidation, *ACS Catal.* 9 (2019) 9751–9763. <https://doi.org/10.1021/acscatal.9b02408>.
- [39] W. Xiao, Y. Guo, Z. Ren, G. Wrobel, Z. Ren, T. Lu, P. Gao, Mechanical Agitation assisted Growth of Large Scale and Uniform ZnO Nanorod Arrays within 3D Multi-channel Monolithic Substrates, *Cryst. Growth Des.* 13 (2013) 3657–3664. <https://doi.org/10.1021/cg400672z>.
- [40] Z. Ren, Y. Guo, G. Wrobel, D.A. Knecht, Z. Zhang, H. Gao, P.X. Gao, Three dimensional koosh ball nanoarchitecture with a tunable magnetic core, fluorescent nanowire shell and enhanced photocatalytic property, *J. Mater. Chem.* 22 (2012) 6862–6868. <https://doi.org/10.1039/c2jm16489b>.
- [41] S. Wang, Z. Ren, W. Song, Y. Guo, M. Zhang, S.L. Suib, P.-X. Gao, ZnO/perovskite core-shell nanorod array based monolithic catalysts with enhanced propane oxidation and material utilization efficiency at low temperature, *Catal. Today* 258 (2015) 549–555. <http://doi.org/10.1016/j.cattod.2015.03.026>.
- [42] Z. Zhang, H. Gao, W. Cai, C. Liu, Y. Guo, P.-X. Gao, In situ TPR removal: a generic method for fabricating tubular array devices with mechanical and structural soundness, and functional robustness on various substrates, *J. Mater.*

- Chem. 22 (2012) 23098. <http://doi.org/10.1039/c2jm34606k>.
- [43] T. Nakamura, M. Misono, Y. Yoneda, Catalytic Properties of perovskite-type mixed oxides  $\text{La}_{1-x}\text{Sr}_x\text{CoO}_3$ , Bull. Chem. Soc. Jpn. 55 (1982) 394–399. <https://doi.org/10.1246/bcsj.55.394>.
- [44] O. Anjaneyulu, S. Ishii, T. Imai, T. Tanabe, S. Ueda, T. Nagao, H. Abe, Plasmon-mediated photothermal conversion by TiN nanocubes toward CO oxidation under solar light illumination, RSC Adv. 6 (2016) 110566. <http://doi.org/10.1039/c6ra22989a>.
- [45] Z. Ren, Y. Guo, P.-X. Gao, Nano-array based monolithic catalysts : Concept , rational materials design and tunable catalytic performance, Catal. Today 258 (2015) 441–453. <http://doi.org/10.1016/j.cattod.2015.01.033>.
- [46] G. Liu, L. Ma, G. Liu, L. Ma, L. Yin, G. Wan, H. Zhu, C. Zhen, Y. Yang, Selective chemical epitaxial growth of  $\text{TiO}_2$  islands on ferroelectric  $\text{PbTiO}_3$  crystals to boost photocatalytic activity, Joule 2 (2018) 2–13. <https://doi.org/10.1016/j.joule.2018.03.006>.
- [47] C. Zhu, A. Wang, W. Xiao, D. Chao, X. Zhang, N.H. Tiep, S. Chen, J. Kang, X. Wang, J. Ding, J. Wang, H. Zhang, H. Fan, In situ grown epitaxial heterojunction exhibits high-performance electrocatalytic water splitting, Adv. Mater. 30 (2018) 1705516. <https://doi.org/10.1002/adma.201705516>.
- [48] F. Zasada, J. Janas, W. Piskorz, M. Gorczyńska, Z. Sojka, Total oxidation of lean methane over cobalt spinel nanocubes controlled by the self-adjusted redox state of the catalyst: Experimental and theoretical account for interplay between the Langmuir-Hinshelwood and Mars-Van Krevelen mechanisms, ACS Catal. 7 (2017) 2853–2867. <http://doi.org/10.1021/acscatal.6b03139>.
- [49] P. Kuiper, G. Kruizinga, J. Ghijsen, G.A. Sawatzky, Character of holes in  $\text{Li}_x\text{Ni}_{1-x}$  and their magnetic behavior, Phys. Rev. Lett. 62 (1989) 221–224. <https://doi.org/10.1103/PhysRevLett.62.221>.
- [50] L. Karvonen, M. Valkeapää, R.S. Liu, J.M. Chen, H. Yamauchi, M. Karppinen, O-K and Co-L XANES study on oxygen intercalation in parasite  $\text{SrCoO}_{3-\delta}$ ,

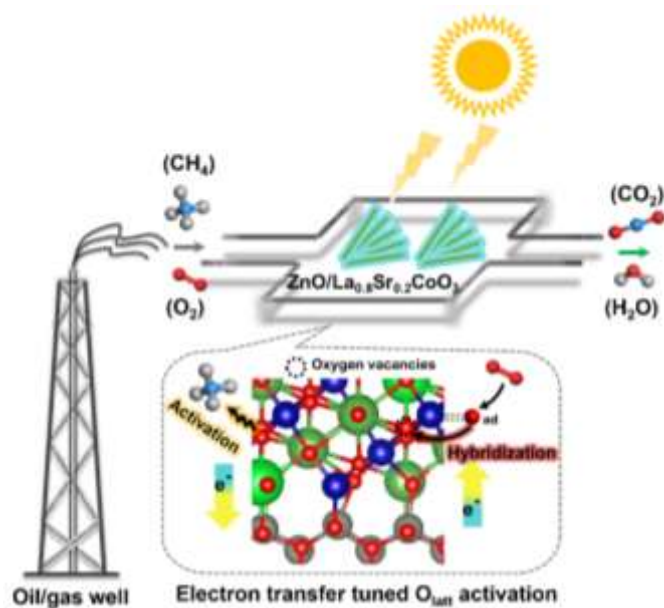
- Chem. Mater. 22 (2010) 70–76. <http://doi.org/10.1021/cm9021563>.
- [51] W.S. Yoon, K.B. Kim, M.G. Kim, M.K. Lee, H.J. Shin, J.M. Lee, J.S. Lee, C.H. Yo, Oxygen contribution on Li-ion intercalation-deintercalation in LiCoO<sub>2</sub> investigated by O K-edge and Co L-edge X-ray absorption spectroscopy, J. Phys. Chem. B 106 (2002) 2526–2532. <http://doi.org/10.1021/jp013735e>.
- [52] M. Sikora, C. Kapusta, K. Knížek, Z. Jiráček, C. Autret, M. Borowiec, C.J. Oates, V. Procházka, D. Rybicki, D. Zajac, X-ray absorption near-edge spectroscopy study of Mn and Co valence states in LaMn<sub>1-x</sub>Co<sub>x</sub>O<sub>3</sub> (x=0-1), Phys. Rev. B 73 (2006) 094426. <http://doi.org/10.1103/PhysRevB.73.094426>.
- [53] X. Li, H. Dai, J. Deng, Y. Liu, Z. Zhao, Y. Wang, H. Yang, C.T. Au, In situ PMMA-templating preparation and excellent catalytic performance of Co<sub>3</sub>O<sub>4</sub>/3DOM La<sub>0.6</sub>Sr<sub>0.4</sub>CoO<sub>3</sub> for toluene combustion, Appl. Catal. A Gene. 458 (2013) 11–20. <http://dx.doi.org/10.1016/j.apcata.2013.03.022>.
- [54] Y. Zhang, Z.-R. Tang, X. Fu, Y.-J. Xu, TiO<sub>2</sub>-Graphene Nanocomposites for Gas-Phase Photocatalytic Degradation of Volatile Aromatic Pollutant: Is TiO<sub>2</sub>-Graphene Truly Different from Other TiO<sub>2</sub>-Carbon Composite Materials, ACS Nano 4 (2010) 7303–7314. <http://doi.org/10.1021/nn1024219>.
- [55] Z. Cai, Y. Kuru, J.W. Han, Y. Chen, B. Yildiz, Surface electronic structure transitions at high temperature on perovskite oxides: The case of strained La<sub>0.8</sub>Sr<sub>0.2</sub>CoO<sub>3</sub> thin films, J. Am. Chem. Soc. 133 (2011) 17696–17704. <https://doi.org/10.1021/ja2059445>.
- [56] J. Ding, X. Lü, H. Shu, J. Xie, H. Zhang, Microwave-assisted synthesis of perovskite ReFeO<sub>3</sub> ( Re : La , Sm , Eu , Gd ) photocatalyst, Mater. Sci. Eng. B 171 (2010) 31–34. <https://doi.org/10.1016/j.mseb.2010.03.050>.
- [57] Q. Meng, W. Wang, X. Weng, Y. Liu, H. Wang, Z. Wu, Active oxygen species in La<sub>n+1</sub>Ni<sub>n</sub>O<sub>3n+1</sub> layered perovskites for catalytic oxidation of toluene and methane, J. Phys. Chem. C 6 (2016) 3259–3266. <http://doi.org/10.1021/acs.jpcc.5b08703>.
- [58] J. Li, R. Hu, J. Zhang, W. Meng, Y. Du, Y. Si, Z. Zhang, Influence of preparation

- methods of  $\text{La}_2\text{CoMnO}_6/\text{CeO}_2$  on the methane catalytic combustion, *Fuel* 178 (2016) 148–154. <https://doi.org/10.1016/j.fuel.2016.03.041>.
- [59] G. Guo, K. Lian, L. Wang, F. Gu, D. Han, Z. Wang, High specific surface area  $\text{LaMO}_3$  (M = Co, Mn) hollow spheres: synthesis, characterization and catalytic properties in methane combustion, *RSC Adv.* 4 (2014) 58699–58707. <http://doi.org/10.1039/C4RA10053K>.
- [60] H. Arandiyana, J. Scott, Y. Wang, H. Dai, H. Sun, R. Amal, Meso-molding three-dimensional macroporous perovskites: A new approach to generate high-performance nanohybrid catalysts, *ACS Appl. Mater. Interfaces* 4 (2016) 2457–2463. <https://doi.org/10.1021/acsami.5b11050>.
- [61] H. Arandiyana, H. Dai, J. Deng, Y. Wang, H. Sun, S. Xie, B. Bai, Y. Liu, K. Ji, J. Li, Three-dimensionally ordered macroporous  $\text{La}_{0.6}\text{Sr}_{0.4}\text{MnO}_3$  supported Ag nanoparticles for the combustion of methane, *J. Phys. Chem.* 118 (2014) 14913–14928. <http://doi.org/10.1021/jp502256t>.
- [62] H. Arandiyana, H. Dai, J. Deng, Y. Liu, B. Bai, Y. Wang, X. Li, S. Xie, J. Li, Three-dimensionally ordered macroporous  $\text{La}_{0.6}\text{Sr}_{0.4}\text{MnO}_3$  with high surface areas: Active catalysts for the combustion of methane, *J. Catal.* 307 (2013) 327–339. <http://doi.org/10.1016/j.jcat.2013.07.013>.
- [63] L. Simonot, F. Garin, G. Maire, A comparative study of  $\text{LaCoO}_3$ ,  $\text{Co}_3\text{O}_4$  and  $\text{LaCoO}_3\text{-Co}_3\text{O}_4$  I. Preparation, characterisation and catalytic properties for the oxidation of CO, *Appl. Catal. B Environ.* 11 (1997) 167–179. [https://doi.org/10.1016/S0926-3373\(96\)00046-X](https://doi.org/10.1016/S0926-3373(96)00046-X).
- [64] M. Crespin, W.K. Hall, The Surface Chemistry of Some Perovskite Oxides, *J. Catal.* 69 (1981) 359–370. [https://doi.org/10.1016/0021-9517\(81\)90171-8](https://doi.org/10.1016/0021-9517(81)90171-8).
- [65] L. Hu, K. Sun, Q. Peng, B. Xu, Y. Li, Surface Active Sites on  $\text{Co}_3\text{O}_4$  Nanobelt and Nanocube Model Catalysts for CO Oxidation, *Nano Res.* 3 (2010) 363–368. <http://doi.org/10.1007/s12274-010-1040-2>.
- [66] J. Zhu, H. Li, L. Zhong, P. Xiao, X. Xu, X. Yang, Z. Zhao, J. Li, Perovskite oxides: Preparation, characterizations, and applications in heterogeneous

- catalysis, *ACS Catal.* 4 (2014) 2917–2940. <http://doi.org/10.1021/cs500606g>.
- [67] W. Si, Y. Wang, Y. Peng, J. Li, Selective dissolution of A-site cations in  $\text{ABO}_3$  perovskites : A new path to high-performance catalysts, *Angew. Chem. Int. Ed.* 54 (2015) 7954–7957. <http://doi.org/10.1002/anie.201502632>.
- [68] Y. Yang, S. Zhang, S. Wang, K. Zhang, H. Wang, J. Huang, S. Deng, B. Wang, Y. Wang, G. Yu, Ball milling synthesized  $\text{MnO}_x$  as highly active catalyst for gaseous POPs removal: Significance of mechanochemically induced oxygen vacancies, *Environ. Sci. Technol.* 49 (2015) 4473–4480. <http://doi.org/10.1021/es505232f>.
- [69] X. Yu, O. Wilhelmi, H.O. Moser, S. V. Vidyaraj, X. Gao, A.T.S. Wee, T. Nyunt, H. Qian, H. Zheng, New soft X-ray facility SINS for surface and nanoscale science at SSLS, *J. Electron Spectrosc.* 144–147 (2005) 1031–1034. <http://doi.org/10.1016/j.elspec.2005.01.256>.
- [70] Z. Ren, V. Botu, S. Wang, Y. Meng, W. Song, Y. Guo, R. Ramprasad, S.L. Suib, P.-X. Gao, Monolithically integrated spinel  $\text{M}_x\text{Co}_{3-x}\text{O}_4$  (M = Co, Ni, Zn) nanoarray catalysts : Scalable synthesis and cation manipulation for tunable low-temperature  $\text{CH}_4$  and CO oxidation, *Angew. Chem. Int. Ed.* 53 (2014) 7223–7227. <http://doi.org/10.1002/anie.201403461>.
- [71] H. Li, F. Qin, Z. Yang, X. Cui, J. Wang, L. Zhang, New Reaction Pathway Induced by Plasmon for Selective Benzyl Alcohol Oxidation on  $\text{BiOCl}$  Possessing Oxygen Vacancies, *J. Am. Chem. Soc.* 139 (2017) 3513–3521. <http://doi.org/10.1021/jacs.6b12850>.
- [72] I. Karakurt, G. Aydin, K. Aydiner, Mine ventilation air methane as a sustainable energy source, *Renew. Sustain. Energy Rev.* 15 (2011) 1042–1049. <http://doi.org/10.1016/j.rser.2010.11.030>.
- [73] R. Jacobs, J. Booske, D. Morgan, Understanding and controlling the work function of perovskite oxides using density functional theory, *Adv. Funct. Mater.* 30 (2016) 5471–5482. <https://doi.org/10.1002/adfm.201600243>.
- [74] Y.J. Fang, J. Sha, Z.L. Wang, Y.T. Wan, W.W. Xia, Y.W. Wang, Behind the

- change of the photoluminescence property of metal-coated ZnO nanowire arrays, *Appl. Phys. Lett.* 98 (2011) 033103. <https://doi.org/10.1063/1.3543902>.
- [75] B.X. Li, H. Zhu, K. Wang, A. Cao, J. Wei, C. Li, Graphene-on-silicon Schottky junction solar cells, *Adv. Mater.* 22 (2010) 2743–2748. [doi:https://doi.org/10.1002/adma.200904383](https://doi.org/10.1002/adma.200904383).
- [76] J. Chen, Z. He, G. Li, T. An, H. Shi, Y. Li, Visible-light-enhanced photothermocatalytic activity of ABO<sub>3</sub>-type perovskites for the decontamination of gaseous styrene, *Appl. Catal. B Environ.* 209 (2017) 146–154. <https://doi.org/10.1016/j.apcatb.2017.02.066>.
- [77] Y. Li, Q. Sun, M. Kong, W. Shi, J. Huang, J. Tang, X. Zhao, Coupling oxygen ion conduction to photocatalysis in mesoporous nanorod-like ceria significantly improves photocatalytic efficiency, *J. Phys. Chem. C* 29 (2011) 14050–14057. <https://doi.org/10.1021/jp202720g>.

## Graphical Abstract



Solar-driven efficient methane oxidation over rational designed  $\text{ZnO}/\text{La}_{0.8}\text{Sr}_{0.2}\text{CoO}_3$  epitaxial heterojunctions under high space velocity continuous flow is demonstrated. The synergy of photothermal and photocatalytic effects further facilitates reversible charge transfer, which promotes the lattice oxygen species activity as well as the fast formation and transformation of oxygen vacancies, resulting in a higher methane oxidation activity.